High-precision quantitative atomic-site-analysis of functional dopants in crystalline materials by electron-channelling-enhanced microanalysis

Shunsuke Muto[1*] and Masahiro Ohtsuka[2]

[1]Electron Nanoscopy Section, Advanced Measurement Technology Center, Institute of Materials and Systems for Sustainability, Nagoya University, Furo-cho, Chikusa-ku, Nagoya 464-8603, Japan.
smuto@imass.nagoya-u.ac.jp

[2]Department of Materials Physics, Graduate School of Engineering, Nagoya University, Furo-cho, Chikusa-ku, Nagoya 464-8603, Japan.
m-ohtsuka@nucl.nagoya-u.ac.jp

*Corresponding author

Abstract

Knowledge of the location and concentration of impurity atoms doped into a synthesized material is of great interest to investigate the effect of doping. This would usually be investigated using X-ray or neutron diffraction methods in combination with Rietveld analysis. However, this technique requires a large-scale facility such as a synchrotron radiation source and nuclear reactor, and can sometimes fail to produce the desired results, depending on the constituent elements and the crystallographic conditions that are being analysed. Thus, it would be preferable to use an element-selective spectroscopy technique that is applicable to any combination of elements. We have established a quantitative method to deduce the occupation sites and their occupancies, as well as the site-dependent chemical states of the doped elements, using a combination of transmission electron microscopy (TEM), energy-dispersive X-ray (EDX) spectroscopy, and electron energy-loss spectroscopy (EELS). The method is based on electron channelling phenomena where the symmetries of the Bloch waves excited in a crystal are dependent on the diffraction condition or incident beam direction with respect to the crystal axes. By rocking the incident electron beam with a fixed pivot point on the sample surface, a set of EDX/EELS spectra are obtained as a function of the beam direction. This is followed by a statistical treatment to extract the atom-site-dependent spectra, thereby quantitatively enabling the estimation of the site occupancies and chemical states of the dopants. This is an extension of the ‘ALCHEMI’ (Atom Location by Channelling Enhanced Microanalysis) method or ‘HARECXS/HARECES’ (High Angular Resolution Channelled X-ray/Electron Spectroscopy), and we further extended the method to be applicable to cases where the crystal of interest contains multiple inequivalent atomic sites for a particular element, applying the precise spectral predictions based on electron elastic/inelastic dynamical scattering theory. After introduction of the conceptual aspects of the method, we describe the extension of the method together with the development of the theoretical calculation method. We then demonstrate several useful applications of the method, including luminescent, ferrite, and battery materials. We discuss the advantages and drawbacks of the present method, compared with those of the recently developed atomic column-by-column analysis using aberration-corrected scanning TEM and high-efficiency X-ray detectors.

Graphical abstract

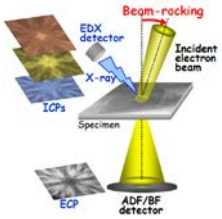

Keywords

Transmission electron microscopy, electron channelling, energy-dispersive X-ray spectroscopy, electron energy-loss spectroscopy, dopant occupancy

1. Introduction

Current technological developments are partly due to progress in understanding how the variation of the physical properties of materials is revealed from the microscopic point of view, particularly in terms of atomic-scale spatial/electronic structural analysis of the materials of interest. Humankind has exploited the useful physical and chemical properties of naturally occurring materials and elements, and created novel or enhanced material properties by combinations of those, such as alloying of metals, and doping of semiconductors and insulators. Novel properties have often been discovered unexpectedly by those experienced in synthesizing materials by trial and error. However, the recent developments in advanced measurement techniques and first-principles theoretical calculations based on the density functional theory [1] have enabled us to propose new materials having novel or better properties without repeated trial-and-error experiments. This is performed by first understanding the origin or mechanism of the known properties based on precise measurements comparable with the theoretical simulations. Then, one or a part of the host atoms are replaced by other elements that could conceivably improve the target property to determine if such replacement would work either experimentally or theoretically. One of the most important pieces of experimental information for this is detailed knowledge of where each constituent resides in the atomic structure of the materials.

The development of high flux X-ray sources such as synchrotron radiation facilities, and modern neutron sources, as well as a sophisticated structural optimization by Rietveld analysis, has led to X-ray and/or neutron diffraction methods becoming widely used techniques [2,3]. These techniques, however, inevitably require samples with uniform structure, because the incident probe (X-ray and neutron) must illuminate a macroscopic area. In addition, the diffraction techniques rely on the Rietveld fit between the experimental and theoretical sets of diffracted peak intensities using structure factors, and can have difficulty distinguishing between different elements if their structure factors happen to be very close to each other, such as occurs in X-ray diffraction of neighbouring elements in the periodic table.

In a semiconductor chip, the compositions, precipitates, grain size, and impurities in the materials should be controlled and optimized to maximize the desired functions at sub-micrometre or even nanometre scales. This means that those materials require characterization at the nanometre scale to confirm if they are correctly synthesized as designed. In this context, microanalysis methods based on transmission electron microscopy (TEM) are important.

Recent progress in aberration-correction technology [4] and high-sensitivity detectors enables the clarification of local atomic structures and atomic column-by-column elemental distributions and chemical information [5]. These include energy-dispersive X-ray (EDX) and electron energy-loss spectroscopy (EELS) in scanning TEM (STEM) using an electron probe focused down to sub-nm size. Although the STEM spectral-imaging technique is powerful enough to visualize the elemental distributions at atomic resolutions, the fact that an electron behaves as a wave in a solid must be considered when quantifying the column-by-column elemental map. Thus, the incident electron is gradually spread over the neighbouring atomic columns when propagating in a solid to thicker regions (> 15–20 nm) even though the electron probe is focused on the subnanometre scale [6]. This effect is more significant when the incident direction of the electron is parallel to a low-order zone axis, which is known as the electron channelling effect. This also suggests that the atomic column-by-column analysis would be highly dependent on the sample quality issues such as sample thickness and the presence of surface damage layers, as well as instrumental alignment issues such as the accuracy of sample orientation, correction of lens astigmatism, and sample drift.

Electron channelling in a crystalline material occurs when an incident electron beam propagates along particular atomic planes or columns, and the channelling effect depends on the direction of the beam with respect to the crystal axes. One of the alternative ways to probe atomically localized electronic states using analytical STEM is to utilize amplitude modulations of electron wavefunctions propagating in a crystal; this does not necessitate focusing the electron beam onto the sample because in crystalline materials, high energy electrons behave as Bloch waves, the symmetries and amplitudes of which can be controlled by selecting an appropriate set of Bragg reflections and the excitation error of each reflection in a TEM [7]. The site-specific energy-dispersive X-ray (EDX) analysis technique that takes advantage of electron channelling effects is known as the atom location by channelled electron microanalysis (ALCHEMI) method [8,9], and is used to evaluate the fraction of host atomic sites occupied by impurities. This method has been extended in a more sophisticated and quantitatively reliable manner, such that the fluorescent X-ray intensities from the constituent elements can be measured as a function of the electron incidence direction, with the particular systematic reflection row excited. This high-angular-resolution electron-channelling X-ray spectroscopy (HARECXS) enables us to derive the impurity/dopant occupancies. More generally, it can also clarify the degree of cation mixing (anti-sites) of the host atoms, by comparing the experimental beam-rocking curves with theoretical simulations [10–13]. An extension of this technique, high-angular-resolution electron-channelling electron spectroscopy (HARECES), records the

EELS instead of EDX [14, 15], thereby elucidating the local chemical states of a given element in different nearest-neighbour atomic environments. In these studies, a multivariate curve resolution (MCR) technique is crucial for separating the overlapping site-specific electron-energy-loss near-edge structures (ELNES) in the angle-dependent spectral data set [16]. Our research group has demonstrated such site-specific EELS measurements in several crystalline materials [17-19].

In the present article, we review microanalysis based on electron channelling phenomena, followed by recent developments in this field associated with current instrumental progress. Then, we introduce several representative examples, particularly focusing on the method combining incident electron beam-rocking and EDX spectroscopy, where the occupation sites and their occupancies of dopant elements are quantitatively determined in functional materials. Finally, we review the future prospects and directions of this technique.

2. Methods

2.1 Fundamentals of electron channelling phenomena

Suppose the simplest case where a monochromatic electron beam is incident to a crystalline solid with only a single Bragg reflection, such that **g** is strongly excited. The electron wave function, $\psi(\boldsymbol{r})$, propagating in the crystal is described as the steady-state solution of Schrodinger's wave equation:

$$\nabla^2\psi(\boldsymbol{r}) + \left(\frac{8\pi^2 me}{\hbar^2}\right)[E + V(\boldsymbol{r})]\psi(\boldsymbol{r}) = 0 \qquad (1)$$

where ∇^2 is the Laplacian operator, m and e are the mass and electric charge of an electron, respectively, E is the incident electron energy, and $V(\mathbf{r})$ is the crystal potential. In the present two-beam case, the total wave function is expressed by a sum of Bloch waves, $b^{(j)}(\mathbf{k}^{(j)}, \mathbf{r})$ (j = 1, 2) [7]:

$$\psi(\boldsymbol{r}) = \sum_{j=1}^{2} \varphi^{(j)} b^{(j)}(\boldsymbol{k}^{(j)}, \boldsymbol{r}) \quad \text{, and} \qquad (2)$$

$$b^{(j)} = \sum_g C_g^{(j)}\left(\boldsymbol{k}^{(j)}\right)\exp(i(\boldsymbol{k}^{(j)} + \boldsymbol{g})\cdot\boldsymbol{r}) \ . \qquad (3)$$

Here, $C_g^{(j)}$ and $\mathbf{k}^{(j)}$ are the solutions of Eq. (1), which reduce to the following two equations under the two-beam approximation:

$$(K^2 - k^2)C_0(\mathbf{k}) + U_{-g}C_g(\mathbf{k}) = 0 \text{ , and} \qquad (4)$$

$$U_g C_0(\mathbf{k}) + (K^2 - (\mathbf{k} + \mathbf{g}))^2 C_g(\mathbf{k}) = 0 \qquad (5)$$

where

$$K^2 = \frac{2meE}{\hbar^2} + U_0 \text{ , and} \qquad (6)$$

$$U_g = \frac{2me}{\hbar^2}\sum_g V(\boldsymbol{r})\exp(-i\boldsymbol{g}\cdot\boldsymbol{r}) \ . \qquad (7)$$

The ratio of the wave amplitudes $C_g^{(j)}/C_0^{(j)}$ are readily calculated at the exact Bragg reflection position and we have

$$b^{(1)} = -i\sqrt{2}\sin(\tfrac{1}{2}\boldsymbol{g}\cdot\boldsymbol{r})\exp(i(\boldsymbol{k}^{(1)}+\tfrac{1}{2}\boldsymbol{g})\cdot\boldsymbol{r}) \quad \text{, and} \qquad (8)$$

$$b^{(2)} = \sqrt{2}\cos(\tfrac{1}{2}\boldsymbol{g}\cdot\boldsymbol{r})\exp(i(\boldsymbol{k}^{(2)}+\tfrac{1}{2}\boldsymbol{g})\cdot\boldsymbol{r}) \quad . \qquad (9)$$

The intensities of the two Bloch waves $|b^{(1)}|^2$ and $|b^{(2)}|^2$ on the two different branches are schematically plotted in Fig. 1 as a function of distance across the atomic planes when we take the origin at an atom which is a centre of inversion in the crystal. The two Bloch waves are oscillating with the period of the Bragg planes with a phase difference of π/2 to each other; thus, each of the two wave fields flows in the direction parallel to the Bragg planes with wave (1) maxima occurring between the atomic planes and nodes at the atomic planes, whereas wave (2) is concentrated on the atomic planes. This phenomenon is termed the planar electron-channelling effect, and is responsible for the anomalous absorption effect [7], because wave (2) is scattered more strongly than wave (1) by the atoms by effects such as ionization and phonon scattering. This effect is also the origin of the site-selective microanalysis described in the next section.

On the other hand, if the incident electron is moving in a direction close to a low-order zone axis of the sample, the electron transmission probability detected at the bottom surface of the sample is very sensitive to the electron incident direction, which is manifested as the electron channelling pattern (ECP); examples of this will be introduced in section 2.7 (Fig. 8). In this case, the incident electron wavefunction branches into Bloch waves with many types of symmetries compatible with the sample crystal symmetry projected along the zone axis, which is termed axial electron channelling [20].

2.2 Atom location by channelled electron microanalysis (ALCHEMI)

Let us again assume the two-beam excitation condition from a different point of view, where only one reciprocal point (Bragg reflection) is strongly excited. Under this condition, the incident electron wavefunction is divided into two Bloch states, whose wavenumbers are confined on closely separated branches (energy levels), termed dispersion planes (Fig. 2). As seen in the previous section, the two Bloch states are characterized by the same periodicity, compatible with that of the Bragg-reflecting planes, and a phase difference of π/2 from each other, in the direction parallel to the diffracting vector **g** (= (*h k l*)). In a simple orthogonal monatomic lattice, one of the Bloch waves propagates through the crystal with its intensity maxima lying on the (*h k l*) planes, while the other Bloch wave propagates with its intensity

maxima kept just in-between the (*h k l*) planes, as shown in Fig. 1. At the exact Bragg condition the two Bloch states are equally excited, though the excitation parameter, which is the relative weight of each Bloch wave determined by the boundary condition [7,15], which varies with the excitation error, *s*, and the total wavefunction is the linear combination of the two Bloch waves $b^{(1)}$ and $b^{(2)}$ in the following form:

$$\psi(r) = \sin(\frac{\beta}{2})b^{(1)}(k^{(1)}, r) + \cos(\frac{\beta}{2})b^{(2)}(k^{(2)}, r). \qquad (10)$$

The parameter β is related to the diffraction condition by $g\xi_g \tan(\Delta\theta) = s\xi_g = \cot(\beta)$, where ξ_g (= K/U_g) is the extinction distance of the operating Bragg reflection **g**, and the other parameters are illustrated in Fig. 2. The changes in the excitation parameters, $\sin(\beta/2)$ and $\cos(\beta/2)$ for Bloch waves (1) and (2), respectively, which are weighting coefficients that represent the degree to which each Bloch wave is excited, are plotted as a function of *s* in Fig. 3. One can thus localize the Bloch waves along specific atom planes or columns by setting *s* to be positive or negative around a certain Bragg condition.

This effect has been utilized in ALCHEMI mainly for EDX, which can provide a direct measure of the site occupation of impurities or dopants. This technique is particularly well suited to layered structures or compounds having superlattice structures where the atomic planes containing the two different host elements are separated and alternatingly stacked if viewed in a specific crystallographic direction. A Bragg reflection corresponding to the periodicity of either of the alternating atomic planes should be selected, and the specimen tilted to the strong two-beam condition, such that the Bloch wave is successively interacting strongly with either of the systematically stacked atomic planes by slightly tilting the sample around the Bragg condition to change the sign of the excitation parameter, *s*. If the fluorescent X-ray intensities of both host elements and the dopant are collected under the conditions of $s > 0$, $s < 0$ and finally at a non-channelling orientation where the electron intensity is uniform for both sites (far away from the two-beam condition), the occupancies of the dopant on the both host sites are estimated using the formulae derived by Spence and Taftø [8,9].

2.3 HARECXS

The original ALCHEMI method relies on three successive measurements of fluorescent X-ray intensities from each element of interest by changing the sample orientation near the operating Bragg condition and finally finding a non-channelling orientation. It is often difficult to obtain sufficient X-ray statistics to draw firm conclusions on the site occupancies of trace elements because the intensity differences in different orientations are often quite small, and

also because the method itself is based on the assumption that the dopant concentrations are too small to significantly perturb the Bloch wave fields by the host elements. In addition, ALCHEMI is only applicable to the cases where the host elements are not intermixed between the corresponding sublattices or when the sublattices of the host elements contain a significant amount of vacancies. Recent development in digital technologies to control the instrument using a computer has enabled us to overcome these drawbacks; this technique is referred to as high-angular-resolution electron-channelled X-ray spectroscopy (HARECXS)

In HARECXS the sample should be orientated in a manner similar to ALCHEMI but with the systematic row of reflections excited, tilting the sample successively over a wide range about the tilting axis perpendicular to the systematic row with a small tilt-angle step and measuring the X-ray spectra. Let us take GaAs having the sphalerite structure as a representative example to explain the general principle. The Ga and As sites in the ZnS structure are located in alternate planes in the stacked {200} planes, as shown in Fig. 4 [21]. The peak positions of the Bloch wave intensities propagating along the planes containing the Ga or As sites can vary, according to the subsequent excitation of the h 0 0 reflections by tilting the incident beam in the direction of the 100 systematic row reflections. The obtained X-ray intensities of Ga-K and As-K with respect to the tilting angle are plotted in Fig. 5, where the measured intensity values were normalized by the values at the non-channelling condition (usually at the end of the measurement and far away from the strong two-beam condition). The X-ray intensities from Ga and As are most different between the orientations of $k/g_{200} = 0$ and 3, where the location of the strongest Bloch wave maxima should be switched from the As planes to Ga planes or vice versa.

Now, fluorescent X-ray intensity profiles can be obtained with respect to the tilting angle for the constituent elements including the impurity elements. The X-ray intensity profiles of the elements are precisely predicted using the Ionized Cross Section Calculator (ICSC) code developed by Oxley and Allen. [22], based on the dynamic electron elastic/inelastic scattering theory, if the atomic structure of the sample is fully known. The calculated cross-sections for the elements on the corresponding experimental condition are also shown as solid lines in Fig. 5. The slight asymmetry of the data points is attributable to the non-uniform sample thickness. The theory and experimental results are in good agreement; thus, one can specify the degree of order by cation mixing in their host sites, dopant occupation sites, and their occupancies by least-square fitting between the experimental and theoretically predicted intensity profiles by adjusting the structural parameters of the model structure.

This method is applicable to rather universal cases with none of the limitations mentioned above, because the structural parameters such as atomic positions and occupancies of constituent elements can be optimized until the best fit between the experimental and calculated HARECXS profiles is obtained. Matsumura's group applied this method to qualitatively clarify the intermixing of the host elements between their occupation sites in an ion track by swift heavy-ion-irradiation to a spinel ceramic material [10,11].

2.4 HARECES

ALCHEMI can be extended to atom site-selective electronic state analysis when applied to TEM-EELS. Taftø and Krivanek. were the first to report an analysis of this type [14] in a study of the valence of iron ions in a chromite spinel. Although channelling EELS has the potential for site-specific measurements in crystals, few applications have been reported in the years after the Taftø study [14]. One reason for this is that the signal-to-noise ratio would usually be very low under the channelling conditions because the EELS entrance aperture should be placed off-axis under the two-beam excitation condition, as shown in Fig. 6 [14], and this could blur out the finer ELNES features. Another reason was the lack of a reliable theoretical calculation for interpreting ELNES. These difficulties are now solved and the technical details and application examples have been reviewed by the present authors' group [15]. Several recent applications are found in [17-19].

It is particularly interesting to investigate spinel ferrites such as $CoFe_2O_4$ and $NiFe_2O_4$; in a set of angular-resolved EELS of the transition metal (TM) elements occupying partly tetrahedral and octahedral sites, each EEL spectrum is expressed by a linear combination of two EEL spectra, one from the tetrahedral site and the other from the octahedral site [19]. The weight of these components varies with the diffraction conditions. Neglecting the insignificant energy dependence of electron channelling effects over the core-loss spectra (in the present case $L_{2,3}$ white-line spectra of TM, which reflect their valence states by the L_2/L_3 intensity ratio), the total intensity of Fe $L_{2,3}$, $I(E)$, for instance, of the spinel ferrites, can be expressed as

$$I(E) \propto N_{tet}\sigma_{tet}I_{tet}(E) + N_{oct}\sigma_{oct}I_{oct}(E) = w_{tet}I_{tet}(E) + w_{oct}I_{oct}(E), \qquad (11)$$

where $I_{tet}(E)$ and $I_{oct}(E)$ are the pure site-specific spectra normalized per atom. N_{oct} and N_{tet} are the number of Fe atoms occupying the octahedral and tetrahedral sites, respectively. Thus, w_{tet} and w_{oct} are the weights of each site-specific spectral component of the measured spectrum. From the experimental spectral data, we resolved ($I_{tet}(E)$, $I_{oct}(E)$) and (w_{tet}, w_{oct}) by an MCR technique [15, 17-19].

The relationship among the experimental spectral set, the spectral components from the two sites, and their weight coefficients is expressed by the following matrix equation:

$$\mathbf{X} = \mathbf{SC} + \mathbf{R}, \qquad (12)$$

where **X**, **S**, **C**, and **R** are respectively $n \times m$, $n \times 2$, $2 \times m$, and $n \times m$ matrices, in which n is the number of EELS detector channels (in the energy-loss axis) used for the analysis and m is the number of steps in the incident beam direction axis. Each column of **X** is the experimental EEL spectrum at a specific incident direction. Similarly, the two columns of **S** correspond to the two EEL spectra from the tetrahedral and octahedral sites. The i-th column of **C** corresponds to the weight coefficients of the tetrahedral and octahedral sites for the experimental spectrum in the i-th incident beam direction. Finally, **R** is the residual matrix, which contains the statistical noise alone when the appropriate **S** and **C** matrices are found. If each component spectrum in **S** is normalized by its integrated intensity, each matrix element in **C** should be proportional to the product of the total cross-section of the core-loss of either site at the specified diffraction condition, and the relative occupancy of the site. However, the solution by MCR based on the alternating least-square (ALS) algorithm [23, 24] is generally not unique and it is usually necessary to lead to the physically correct solution by imposing additional constraints such as non-negativity on all the entries in both **S** and **C**. Instead, concurrent measurement of EELS/EDX will solve the problem, by deriving the site occupancies from the HARECXS analysis, which is demonstrated in the later section.

2.5 Theoretical simulation of fluorescent X-ray emission/electron energy-loss cross sections based on dynamic electron elastic/inelastic scattering theory

HARECXS/HARECES require theoretical simulations of the inelastic-scattering cross-sections as functions of the tilting angle of the incident beam with respect to the specified crystal orientation. Theoretical calculation schemes for both HARECXS and HARECES should be formulated based on the electron-inelastic-scattering theory with the dynamic electron diffraction effects incorporated, although the theoretical treatments are slightly different for HARECXS and HARECES. X-ray emissions associated with the inelastic scattering events are closely related to the corresponding core-electron excitation (inner-shell ionization). However, the X-rays, once emitted, hardly interact with the sample until they reach the detector, whereas the inelastically scattered electrons are subject to repeated elastic scattering in the sample until they exit from the bottom surface of the sample. The theory of HARECES is hence a more general case, while that of HARECXS can be rather simplified.

There are two theoretical routes to treat the inelastic scattering of an incident fast electron in the material, and they achieve the same goal. Although Yoshioka's approach [25, 26] is one of the best-known treatments, it is slightly circuitous. His goal is to include the inelastic scattering effect in the elastic-scattering wavefunction as small perturbations by the absorption of elastically scattered electrons, and thus the inelastic-scattering cross-section is derived from the amount of absorbed electrons. Instead, van Hove's approach [27-29], in which the inelastic-scattering cross-section is factorized to calculate a quantity termed dynamic form factor (DFF), seems to be mathematically straightforward. In this paper, the latter is selected as a starting equation.

The double differential cross-section (DDCS) of inelastic electron scattering (i.e., ELNES) was formulated by taking into account the incoming and outgoing fast electrons using the direct products between the incident fast electron waves and scattered electron waves for the initial and final states of all the particles (nuclei or electrons) in the material.

Under the first-order Born approximation, we first assume the single-inelastic-scattering approximation and the kinematical approximation for incident fast electrons. In this case, the fast electrons before and after the inelastic scattering can be described as single plane waves with their wave vectors $\mathbf{k}_i$ and $\mathbf{k}_f$ related by the momentum transfer $\hbar\mathbf{q} = \hbar(\mathbf{k}_f - \mathbf{k}_i)$, and the DDCS of ELNES can be written as

$$\begin{aligned}\frac{\partial^2\sigma}{\partial E\partial\Omega} &= \frac{2\pi}{\hbar}\sum_i\sum_f |<\psi_{\text{in}}|\otimes<\phi_i|V(\mathbf{r}-\boldsymbol{\tau})|\phi_f>\otimes|\psi_{\text{out}}>|^2\,\delta(E_f-E_i-E) \\ &= \frac{m^2e^4}{4\pi^2\varepsilon_0^2\hbar^4}\frac{k_f}{k_i}\frac{S(\mathbf{q},E)}{q^4}\end{aligned} \quad , \qquad (13)$$

where the DFF is given by

$$S(\mathbf{q},E) = \sum_i\sum_f |<\phi_i|\exp(i\mathbf{q}\cdot\boldsymbol{\tau})|\phi_f>|^2\,\delta(E_f-E_i-E) \quad . \qquad (14)$$

Here, $<\psi_{\text{in}}| = \exp(i\mathbf{k}_i\cdot\mathbf{r})$ and $<\psi_{\text{out}}| = \exp(i\mathbf{k}_f\cdot\mathbf{r})$ are the incoming and outgoing fast electron waves, respectively, $<\phi_i|$ and $<\phi_f|$ are the initial and final many-electron states in the material, respectively, $\mathbf{r}$ is the coordinate of the fast electron, $\boldsymbol{\tau}$ contains the coordinates of all the particles (nuclei or electrons) in the material, $E = \hbar^2(k_f^2 - k_i^2)/2m$ is the energy loss of the fast electron, m is the electron mass including the relativistic correction, and ε_0 is the permittivity of vacuum. The interaction term in the Hamiltonian, $V(\mathbf{r}-\boldsymbol{\tau}) = e^2/4\pi\varepsilon_0|\mathbf{r}-\boldsymbol{\tau}|^2$.

However, a crystalline specimen essentially diffracts an incident electron plane wave into many diffracted plane waves, and thus the incoming and outgoing waves cannot be represented by single plane waves. As the result, the interference (i.e., cross terms) between individual

plane-wave components of the incoming and outgoing waves should be included in the DDCS formula, and thus the DFF is extended to the mixed dynamic form factor (MDFF) given by

$$S(\mathbf{q},\mathbf{q}',E)=\sum_i\sum_f <\phi_i|\exp(i\mathbf{q}\cdot\boldsymbol{\tau})|\phi_f><\phi_f|\exp(-i\mathbf{q}'\cdot\boldsymbol{\tau})|\phi_i>\delta(E_f-E_i-E), \qquad (15)$$

where $\mathbf{q} = \mathbf{k}_f - \mathbf{k}_i$, $\mathbf{q}' = \mathbf{k}_f' - \mathbf{k}_i'$, $\mathbf{k}_i$ and $\mathbf{k}_i'$ are wavevectors of plane wave components of the incoming wave, and $\mathbf{k}_f$ and $\mathbf{k}_f'$ are those of the outgoing wave. If we include dynamic elastic-scattering effect into the incoming and outgoing waves, both sets of plane waves can take the Bloch-wave form. In this case, $\mathbf{q} = \mathbf{k}^{(l)} - \mathbf{k}^{(j)} + \mathbf{h} - \mathbf{g}$, $\mathbf{q}' = \mathbf{k}^{(l')} - \mathbf{k}^{(j')} + \mathbf{h}' - \mathbf{g}'$, and $\mathbf{k}^{(i)}$ are wavevectors excited on the i-th branch (dispersion surface) of the Bloch states, with the superscripts j and j' (l and l') representing the incoming (outgoing) waves; $\mathbf{g}$ and $\mathbf{g}'$ ($\mathbf{h}$ and $\mathbf{h}'$) are reciprocal lattice vectors of operating incoming (outgoing) waves, respectively. Summation over the operating diffracted waves and $\mathbf{q}$ and $\mathbf{q}'$ associated with the possible scattering paths for the atoms at a specific site of interest within the unit-cell simulates the atom site-selective DDCS for a specimen with thickness t [30]:

$$\frac{\partial^2\sigma_{site}}{\partial E\partial\Omega}=\frac{1}{N_u}\sum_{u\subset site}^{unitcell}\sum_{j,j'}\sum_{g,g'}\sum_{l,l'}\sum_{h,h'}T^{jj'll'}(t)Y^{jlj'l'}_{ghg'h'}\frac{S_u(\mathbf{q},\mathbf{q}',E)}{q^2q'^2}\exp[i(\mathbf{q}-\mathbf{q}')\cdot\mathbf{u}], \qquad (16)$$

$$T^{jj'll'}(t)=\frac{\cosh(\delta t/2)\sin(\Delta t/2)+i\sinh(\delta t/2)\cos(\Delta t/2)}{\Delta t/2+i\delta t/2}, \qquad (17)$$

$$Y^{jlj'l'}_{ghg'h'}=\alpha^{(j)}C_g^{(j)}\varepsilon^{(l)*}D_h^{(l)*}\alpha^{(j')*}C_{g'}^{(j')*}\varepsilon^{(l')*}D_{h'}^{(l')}, \quad \text{and} \qquad (18)$$

$$\Delta=\gamma^{(j)}-\gamma^{(j')}-(\gamma^{(l)}-\gamma^{(l')}),\ \ \delta=\eta^{(j)}-\eta^{(j')}-(\eta^{(l)}-\eta^{(l')}), \qquad (19)$$

where $C_g^{(i)}$ ($D_h^{(l)}$) is the Fourier coefficient associated with the elastic scattering vector $\mathbf{g}$ ($\mathbf{h}$) for i-th (l-th) Bloch states with its excitation amplitude $\alpha^{(i)}$ ($\varepsilon^{(l)}$) of the incoming (outgoing) wave. $T_{jj'll'}$ is a thickness-dependent function that describes the specimen thickness effect and the nominal absorption, with the real (γ) and imaginary (η) parts of the eigenvalues of the Bloch states introduced [30]. N_u is the number of atoms in the unit-cell, $\mathbf{u}$ is the atom position in the unit cell, and the term $\sum_u^{unitcell}\exp[i(\mathbf{q}-\mathbf{q}')\cdot\mathbf{u}]$ acts as a structure factor determining the atomic site-selectivity. This formula can be derived from the first line of Eq. (13) with the incoming and outgoing Bloch waves, $<\psi_{\text{in}}| = \sum_j\alpha^{(j)}\sum_g C_g^{(j)}\exp[i(\mathbf{k}^{(j)}+\mathbf{g})\cdot\mathbf{r}]$ and $<\psi_{\text{out}}| = \sum_l\varepsilon^{(l)}\sum_g D_g^{(l)}\exp[i(\mathbf{k}^{(l)}+\mathbf{h})\cdot\mathbf{r}]$.

Analytical calculations of Eqs. (16)–(19), where the incoming and outgoing fast electrons were treated within the two-beam approximation, provided a good qualitative explanation for experimentally observed electron channelling effects [15]. However, a full many-beam calculation is a time-consuming task, because octupole summation over $\mathbf{g}$, $\mathbf{g}'$, $\mathbf{h}$, $\mathbf{h}'$, j, j', l, and l' is contained inside the single summation over to atomic site u, is shown in Eq. (16). If we

assume *n* beams and *m* atoms for a selected site, the order of this operation is $O(n^8 \times m)$. The MATS code developed by Rusz *et al* [32] allows highly accurate calculations at much lower computational costs by skilfully reducing the non-significant terms.

In contrast to the HARECES theory, the HARECXS theoretical calculation is greatly simplified. In the case of HARECXS measurement where incident angle of the beam is varied (i.e., beam-rocking, not specimen-rocking), the geometry between an emission point of the characteristic X-ray and the EDX detector is unchangeable, so that the X-ray diffraction effect is negligible. If the variation of X-ray emission intensity with respect to orientation is assumed as a mere scaling factor, a characteristic X-ray intensity can be assumed to be proportional to the total intensity of inelastically scattered electrons corresponding to the operating core-electron excitation, i.e., total inelastic scattering cross-section for the inner-shell ionization. This mean that the HARECXS signal approximately corresponds to the HARECES signal with an EELS detector covering whole solid angles. Therefore, the dynamic elastic scattering of fast electrons after the inelastic scattering can be negligible, and Eq. (16) is simplified as

$$\frac{\partial^2 \sigma_{site}}{\partial E \partial \Omega} = \frac{1}{N_u} \sum_{u \subset site}^{unitcell} \sum_{j,j'} \sum_{g,g'} B^{jj'}(t) C_g^{(j)} C_{g'}^{(j')*} \frac{S_u(\mathbf{q},\mathbf{q}',E)}{q^2 q'^2} \exp[i(\mathbf{q}-\mathbf{q}')\cdot\mathbf{u}], \text{ and} \qquad (20)$$

$$B^{jj'}(t) = \alpha^{(j)} \alpha^{(j')*} \frac{\exp[i(\gamma^{(j)} - \gamma^{(j')} + i\eta^{(j)} + i\eta^{(j')})t] - 1}{i(\gamma^{(j)} - \gamma^{(j')} + i\eta^{(j)} + i\eta^{(j')})t}, \qquad (21)$$

where $\mathbf{q} = \mathbf{k}_f - \mathbf{k}^{(j)} - \mathbf{g}$ and $\mathbf{q}' = \mathbf{k}_f - \mathbf{k}^{(j')} - \mathbf{g}'$. Thus, the total inelastic-scattering cross-section for the atoms at a specific site of interest can be obtained by

$$\begin{aligned} \sigma_{site} = & \frac{1}{N_u} \sum_{u \subset site}^{unitcell} \sum_{j,j'} \sum_{g,g'} B^{jj'}(t) C_g^{(j)} C_{g'}^{(j')*} \exp[i(\mathbf{k}^{(j')} - \mathbf{k}^{(j)} + \mathbf{g}' - \mathbf{g})\cdot\mathbf{u}] \\ & \times \int\int k_f \frac{S_u(\mathbf{k}_f - \mathbf{k}^{(j)} - \mathbf{g}, \mathbf{k}_f - \mathbf{k}^{(j')} - \mathbf{g}', E)}{|\mathbf{k}_f - \mathbf{k}^{(j)} - \mathbf{g}|^2 |\mathbf{k}_f - \mathbf{k}^{(j')} - \mathbf{g}'|^2} d\Omega \, dk_f \end{aligned} . \qquad (22)$$

Here, if we assume $\mathbf{k}_0 \approx \mathbf{k}^{(j)} \approx \mathbf{k}^{(j')}$ where $\mathbf{k}_0$ is the incident wavevector in vacuum, the result of angular integration does not depend on the incident wavevector $\mathbf{k}_0$, and thus the above equation is simplified to

$$\begin{aligned} \sigma_{site} = & \frac{1}{N_u} \sum_{u \subset site}^{unitcell} \sum_{j,j'} \sum_{g,g'} B^{jj'}(t) C_g^{(j)} C_{g'}^{(j')*} \exp[i(\mathbf{g}' - \mathbf{g})\cdot\mathbf{u}] \\ & \times \int\int k_f \frac{S_u(\mathbf{k}_f - \mathbf{k}_0 - \mathbf{g}, \mathbf{k}_f - \mathbf{k}_0 - \mathbf{g}', E)}{|\mathbf{k}_f - \mathbf{k}_0 - \mathbf{g}|^2 |\mathbf{k}_f - \mathbf{k}_0 - \mathbf{g}'|^2} d\Omega \, dk_f \qquad , \qquad (23) \\ = & \frac{1}{N_u} \sum_{u \subset site}^{unitcell} \sum_{j,j'} \sum_{g,g'} B^{jj'}(t) C_g^{(j)} C_{g'}^{(j')*} \exp[i(\mathbf{g}' - \mathbf{g})\cdot\mathbf{u}] \, f_u(\mathbf{g},\mathbf{g}') \\ = & \sum_{j,j'} \sum_{g,g'} B^{jj'}(t) C_g^{(j)} C_{g'}^{(j')*} W_{g,h} \end{aligned}$$

where $f(\mathbf{g}, \mathbf{g}')$ is the atomic scattering factor for inner-shell ionization, and $W_{g,h}$ is the Fourier coefficient of the so-called transition potential for ionization of the atoms of interest [33, 34]. As previously mentioned, the angular integration is performed for all scattering angles, and thus the local approximation, $f(\mathbf{g}, \mathbf{g}') \approx f(\mathbf{g} - \mathbf{g}', 0)$ and $W_{g,g'} \approx W_{g-g',0}$, can be applied without significant errors. The values of these scattering factors with the local approximation, $f(\mathbf{g} - \mathbf{g}', 0)$, are parametrized by a simple mathematical function and the fitted parameters are tabulated for various elements and inner-shells by Oxley and Allen [34].

In HARECXS measurements the optimum specimen thickness is around 100–150 nm, which is relatively larger than the optimum value for an HARECES case (i.e., EELS). Therefore, the contribution of inelastically scattered electrons cannot be negligible. This inelastic-scattering contribution is mainly caused by thermal diffuse scattering (TDS), which is typically treated as a phenomenological absorption of elastic electrons in the Bloch-wave calculations based on Yoshioka's approach [25]. Neglecting the diffraction effect of TDS electrons, the TDS electron wavefunction takes a single plane waveform, and its contribution to the total inelastic scattering is roughly modelled by [35]

$$\sigma'_{site} = \left[1 - \sum_{j,j'} \sum_{g} B^{jj'}(t) C_g^{(j)} C_g^{(j')*} \right] W_{0,0}, \qquad (24)$$

where the second term in the square bracket is the integrated intensity of the elastically scattered electron wavefunction, and thus the term in square brackets is the integrated intensity of absorbed electrons (i.e., TDS electrons).

By using the above results, a simulated characteristic X-ray intensity $I_\kappa(\mathbf{k}_0)$ can be expressed by:

$$I_\kappa(\mathbf{k}_0) = Q \cdot T \cdot D_\kappa \cdot \left(\frac{\Omega}{4\pi} \right) \cdot \omega_\kappa \cdot (\sigma_{site} + \sigma'_{site}), \qquad (25)$$

where Q is the incident electron beam current, T is the live dwell time, and Ω is the effective solid angle of the EDX detector. D_κ is the efficiency of the detector in a selected energy range, and ω_κ is the X-ray fluorescence yield for the X-ray signal from element κ. If X-ray absorption within the specimen must be taken into account, then Eqs. (23) and (24) should be modified as [36]:

$$\sigma_{site} = \sum_{j,j'} \sum_{g,g'} B'^{jj'}(t) C_g^{(j)} C_{g'}^{(j')*} W_{g,h}, \text{ and} \qquad (26)$$

$$\sigma'_{site} = \left[\left(\frac{1 - \exp(-Rt/\lambda_X)}{Rt/\lambda_X} \right) - \sum_{j,j'} \sum_{g} B'^{jj'}(t) C_g^{(j)} C_g^{(j')*} \right] W_{0,0}, \text{ where} \qquad (27)$$

$$B'^{jj'}(t) = \alpha^{(j)}\alpha^{(j')*}\frac{\exp[i(\gamma^{(j)} - \gamma^{(j')} + i\eta^{(j)} + i\eta^{(j')} + iR/\lambda_X)t] - 1}{i(\gamma^{(j)} - \gamma^{(j')} + i\eta^{(j)} + i\eta^{(j')} + iR/\lambda_X)t}. \qquad (28)$$

Here, $R = \cos\varphi/\sin(\varphi + \theta)$, where θ is the detector take-off angle and φ is the goniometer tilt-angle towards the detector, and the detector is perpendicular to the goniometer tilt axis. The mean free path for absorption of the characteristic X-rays is $\lambda_X = 1/(\mu\rho)$, where μ is the mass absorption coefficient and ρ the density. It should be noted that this treatment assumes that X-ray scattering occurs in the specimen.

As previously explained, in EDX simulations, the local approximation of atomic scattering factor for ionization, and the kinematical approximation for the outgoing wave after inelastic scattering are justified. As the result, the octuple summation in Eq. (16) for the EELS case is reduced to the quadruple summation in Eq. (26) for EDX, and thus the computational cost of an EDX simulation is much smaller than for EELS.

2.6 Statistical ALCHEMI (St-ALCHEMI)

The original ALCHEMI method is simple and provides a useful insight into the impurity occupation sites, although it is not necessarily quantitatively accurate because the equation to derive the occupancy includes a subtraction operation in the denominator. On the other hand, HARECXS requires *a priori* knowledge about the crystal structure of the material for the theoretical X-ray profile prediction. Thus, the statistical ALCHEMI/HARECXS method was proposed to quantitatively determine the site occupancies of substitutional dopants or impurities on the host sites in an even simpler and more precise way [37, 38]. The method requires no detailed structural parameters about the host crystal, such as the lattice parameters and precise fractional host atom positions in the unit cell, but assumes that there is no site mixing between the host atoms.

It is seen that the different X-ray intensities emitted from each site depends on the crystal orientation, and accordingly the characteristic X-ray intensities from the host elements and substitutional impurities vary with the orientation, depending on which site they occupy. If the fractional occupancy f_{ix} of impurity x on the type i host site, the X-ray intensity I_i of host atoms of type i, for instance, under dynamical diffraction conditions may be written as

$$I_i = \frac{\text{const.} \times (n_i - \sum_x c_x f_{ix})}{k_i} F_i, \qquad (29)$$

where c_x is the concentration of impurity x, n_i is the fractional concentration of the type i host element among the total host sites prior to impurity atoms of type x being accommodated and f_{ix} is the fraction of impurity x occupying the i-site. k_i is the k-factor of the type i host element and

F_i is the multiplicative factor per atom to scale the ionization cross-section under kinematic diffraction conditions to that observed under dynamic conditions, expressed as the sum of a dynamic component and a kinematic (dechannelled) component [39]. The X-ray intensity I_x for impurity x, on the other hand can be written as

$$I_x = \frac{const. \times c_x}{k_k} \sum_i f_{ix} F_i \quad , \qquad (30)$$

if the dynamic enhancement factor F_i^x for impurity x on sites i is assumed to be equal to F_i. This assumption is reasonable if monitored excitations are localized compared with possible fluctuations in the fast electron probability density across the various sites. Substituting the value for F_i from Eq. (29) for F_i in Eq. (30), the X-ray intensity I_x for impurity x can then be written in the following form [37, 38] as a function of X-ray intensity I_i of host element i,

$$I_x = \frac{c_x}{k_k} \sum_i \frac{f_i k_i I_i}{(n_i - \sum_x c_x f_{ix})} = \sum_i \alpha_{ix} I_i + \beta_x, \qquad (31)$$

where

$$\alpha_{ix} = \frac{c_x}{k_k} \frac{f_i k_i}{(n_i - \sum_x c_x f_{ix})}. \qquad (32)$$

Eq. (29) only holds in cases where the impurity concentrations are not too high to significantly perturb the Bloch wave field of the host crystal lattice. The additional constant offset β_x has been introduced as an extra fitted parameter, to account for differences in interaction delocalization and errors in background subtractions. This point is discussed in detail in [40], and this additional parameter would ensure the stability of the method. If many datasets of X-ray intensities from the cation elements are collected by tilting a sample by a few degrees at the same spot, α_{ix} can be derived from Eq. (31) by a multivariate linear regression. Then, c_x and f_{ix} can be derived utilizing $\sum_i f_{ix} = 1$ as

$$c_x = \sum_i \frac{\alpha_{ix} n_i}{(\sum_x \alpha_{ix} + k_i / k_x)}, \quad f_{ix} = \frac{\alpha_{ix} n_i}{c_x (\sum_x \alpha_{ix} + k_i / k_x)}. \qquad (33)$$

The uncertainties in c_x and f_{ix} for multiple impurities are readily estimated from the error propagation principle:

$$(\delta c_x)^2 = \sum_i \left[- \frac{\alpha_{ix} n_i}{(\sum_x \alpha_{ix} + k_i / k_x)^2} + \frac{n_i}{(\sum_x \alpha_{ix} + k_i / k_x)} \right]^2 (\delta \alpha_{ix})^2 \quad , \text{and} \qquad (34)$$

$$(\delta f_{ix})^2 = \frac{1}{c_x^2}\left[-\frac{\alpha_{ix} n_i}{(\sum_x \alpha_{ix} + k_i / k_x)^2} + \frac{n_i}{(\sum_x \alpha_{ix} + k_i / k_x)}\right]^2 (\delta\alpha_{ix})^2 + \left(\frac{\delta c_x}{c_x^2}\right)^2 \left[\frac{\alpha_{ix} n_i}{(\sum_x \alpha_{ix} + k_i / k_x)}\right]^2 . \quad (35)$$

In principle, one can obtain statistically sufficient accuracies in estimating the site occupancies of the dopant if 20–30 EDX spectra are collected at random crystal orientations. However, modern STEM-EDX systems allow us to automatically collect a sufficient number of data points using a digital beam controlling function of STEM mode, which is introduced in the next section.

2.7 Instrumental requirements for automatic beam-tilting measurement

In our measurement system, TEM-EDXS analysis is performed using a JEM-2100 S/TEM (Jeol, Japan) microscope operated in the beam-rocking mode at 200 keV, and equipped with a Dry SD30GV EDXS silicon drift detector (Jeol, Japan). The STEM has an optional beam-rocking function in the ASID STEM controlling window. In beam-rocking mode, the annular dark-field (ADF) detector collects the two-dimensional scattering intensities with respect to the beam tilt angle as shown in Fig. 7(b), compared with the conventional scanning mode (Fig. 7(a)). This is an electron channelling pattern (ECP), which reflects the amount of thermal diffuse scattering (TDS: mainly due to the phonon scattering) subject to Bragg reflections through dynamical electron scattering effects. ECP is utilized for setting the sample orientation from its geometrical symmetry. The data acquisition was performed using the Spectral Image function and line scan function in the Thermo NSS software (Thermo Fischer Scientific Inc., USA) [41] for 2D measurement and 1D tilting measurement of a systematic row of reflections, respectively. A collimated incident beam with a convergence semi-angle of approximately 2 mrad (measured from the diffraction pattern) is used; the beam size can be adjusted by selecting the size of condenser aperture, approximately ranging between 300 nm and 1 μm in diameter in the present hardware system. A smaller beam size is feasible in principle, but it is practically difficult to keep the pivot point fixed on a sample.

By operating the STEM in beam-rocking mode, the Spectral Image method collects EDX spectra as a function of beam tilting angles in the *x*- and *y*-directions and display elemental intensity distribution, $I_A(\mathbf{k}_i)$ (the intensity of *i*-th pixel) for an specified element, A, where $\mathbf{k}_i$ is the incident wavenumber vector corresponding to the *i*-th incident beam angle. The intensity distribution pattern is called an ionization channelling pattern or incoherent channelling pattern (ICP). The experimental ECP for $BaTiO_3$ and ICPs of Ba-L, Ti- K_α, and O-K_α around the [100] and [110] zone axes are shown in Figs. 8(a) and (b), respectively.

The advantage of using ECP and ICP for HARECXS measurement is that (i) no instrumental modification is necessary, (ii) a large number of data sampling points (> 4,000) can be collected with high efficiency by the same operation procedure of STEM spectral imaging by using beam-rocking mode instead of parallel scanning mode, (iii) it is also possible to carry out conventional HARECXS measurements with a systematic row of reflections successively excited by applying the line scan analysis mode of the EDX analyser, and (iv) multiple detectors such as EDX, EELS, and CL can be incorporated on a single analysis software platform and thus concurrent measurements in a unified operation system are feasible. Owing to the user-friendly GUI of the controlling software, the operation is simple and intuitive.

In cases where the microscope used does not have beam-rocking mode, the same operation is realized by using the beam controlling software QED, running on the Gatan Microscope Suite (Gatan Inc.), supplied by HREM Research Inc. [42]; for S/TEMs manufactured by FEI Company, TIA scripting, open-source code can control all the S/TEM functions via a PC [43]. The sequential EDX/EELS data acquisitions with successive incident beam tilting were carried out using the scripting program TIA running on the TEM imaging and analysis platform. This open source software enabled full digital control of the FEI TEMs and attached detectors.

2.8 Selection of orientation

HARECX(E)S and St-ALCHEMI methods are generally applicable to any orientation of the sample, although there is a selection criterion to guarantee better precision in the measurement. Because HARECXS and St-ALCHEMI methods are respectively based on planar and axial channelling effects, it is best to select the sample orientation where the different host elements are separately viewed in the projected structure, belonging to different atomic planes viewed end-on; this is perpendicular to the operating Bragg reflection vector for HARECX(E)S, and to different atomic columns aligned along the projected direction for St-ALCHEMI, where the site-specific Bloch wave field varies most with the incident beam direction change. These criteria are closely related to accuracy evaluation based on the statistical theories, which is discussed in section 2.11.

In the usual EDX analysis, absorption of X-ray emission is supposed to be considered depending on the sample-detector geometry, sample thickness, and sample composition. In the St-ALCHEMI technique, the absorption effects can be incorporated into the selection of the Cliff-Lorimer *k*-factor and do not have to be taken into account, as discussed in the next section.

2.9 Effects of sample thickness, inaccuracies of *k*-factors, and beam convergence on quantified parameters

Figure 9 shows the GaAs structure projected along the [310] direction [21] and the corresponding calculated through-thickness ICPs of the Ga-K, As-K, and Si-K emission around the [310] zone axis obtained from a Si-doped GaAs crystal with 1 at.% Si substituted both for Ga and As sites with equal occupancies. In the projected atomic structure along the [310] direction (Fig. 9(a)), the Ga and As atomic columns are well separated, showing polarity (non-centrosymmetric) in the [001] direction, which is reflected in the asymmetric ICPs of Ga- and As-K lines over all the thicknesses. Si-K ICPs show the averaged contrast of Ga-K ICPs and As-K ICPs, because Si atoms occupy both Ga and As sites equally. As shown in Eq. (25), the X-ray ICPs are constructed by the contribution of elastically-scattered electrons and the contribution of TDS electrons. The former exhibits site-dependent channelling contrast, whereas the latter shows site-independent contrast. As the specimen thickness is increased, the site-independent contrast should be enhanced because the number of absorbed electrons increased with thickness. However, the present simulation suggests that the site-dependent contrast is still clearly observed at thicknesses up to 200 nm. In addition, the ICPs improve their sharpness with increasing thickness, although the contrast is no longer sensitive to the sample thickness for cases of more than 100 nm. This suggests that precise thickness measurement is not demanding for comparison between experimental results and their corresponding theoretical simulations.

By applying the St-ALCHEMI method (Eqs. (31)-(35)) to the set of calculated X-ray ICPs, the Si-K ICPs turned out to be well reproduced by the 1:1 linear combination of the Ga-K and As-K ICPs as expected, as shown in the right-most column of Fig. 9(b). The corresponding estimated values of c_{Si} and $f_{i,\mathrm{Si}}$ (i = Ga, As) are shown as functions of thickness in Figs. 10(a) and (b), respectively. In the present simulation, k_i/k_x was slightly adjusted for c_{Si} and $f_{i,\mathrm{Si}}$ to yield the expected values at the thickness of 25 nm. The variations of these values with increasing thickness are less than 10% and 1% for c_{Si} and $f_{i,\mathrm{Si}}$, respectively, which proves that the St-ALCHEMI method is applicable to the wide range of typical TEM sample thickness.

Let us now discuss the accuracies of impurity concentration and its occupancies deduced by the St-ALCHEMI method, assuming a typical case where the impurity concentration is less than 10%; within the assumption of St-ALCHEMI method in which the concentration of an impurity atom is small enough compared with the host elements not to perturb the Bloch wave field of the host lattice too much. To do this, we should mainly consider the uncertainties

propagated from the error of *k*-factors as the affecting factors, which can be readily estimated from Eq. (33) by the error propagation principle:

$$(\delta c_x)^2 = \sum_i \left[-\frac{\alpha_{ix} n_i}{(\sum_x \alpha_{ix} + k_i / k_x)^2} \right]^2 [\delta(k_i / k_x)]^2, \quad \text{and} \tag{36}$$

$$(\delta f_{ix})^2 = \frac{1}{c_x^2} \left[-\frac{\alpha_{ix} n_i}{(\sum_x \alpha_{ix} + k_i / k_x)^2} \right]^2 [\delta(k_i / k_x)]^2 + \left(\frac{\delta c_x}{c_x^2} \right)^2 \left[\frac{\alpha_{ix} n_i}{(\sum_x \alpha_{ix} + k_i / k_x)} \right]^2, \tag{37}$$

where $\delta(k_i/k_x)$ is the uncertainty of the Cliff-Lorimer *k*-factor with k_i/k_x, representing the *i*-th host element and *x*-th impurity element. If characteristic X-ray lines ranging from 0.5–10 kV are selected for analysis, k_i/k_x typically ranges over 0.35–2.21 (for atomic number Z = 8–79). The typical values of regression coefficients, α_{ix}, are generally less than 0.1 in the case where the concentration of impurity element is less than 10%. Under these assumptions, the term in the square bracket in Eq. (36) is much less than unity, and hence even an uncertainty of the Cliff-Lorimer *k*-factor of ~30% would yield a deviation of c_x of less than 10%. On the other hand, Eq. (37) suggests that the uncertainty of f_{ix} depends on the c_x, and the smaller c_x causes the larger error of f_{ix}. If c_x = 3 at.% is assumed, the uncertainty of f_{ix} is less than 0.1 even if the uncertainty of k_i/k_x is as large as 30%. For above-mentioned model simulation with 100-nm-thickness, if we assume the relative error of ±10% for the Cliff-Lorimer *k*-factor k_{Ga}/k_{Si}, the variations of c_x and f_{ix} (i = Ga, As, x = Si) values can be estimated as shown in Figs. 11(a) and (b), respectively. It is seen that the uncertainties of c_x and f_{ix} are less than 6% for the 10% inaccuracies of k_i/k_x. It should be noted that the above estimated inaccuracies of the parameters can vary depending on the parameter used and the accuracies must be checked for individual cases using Eqs. (34)–(37).

Another parameter affecting the stability of the parameters deduced by the St-ALCHEMI method could be the convergence semi-angle of the incident electron beam, which can blur the ICP contrast. If the beam convergence is less than a few mrad, the convergent beam can be considered as the incoherent superposition of plane-waves with different incident angles because there is little interference (overlap) between diffracted disks in the diffraction plane. The theoretically simulated ICP can accurately reproduce the experimental one by convolution of the ICP for a parallel beam with a Gaussian having a FWHM of the convergence angle. In the case of larger convergence angles where the diffracted discs are partially overlapped, coherent interference between the diffracted beams occurs, so that the position dependence of a convergent beam probe may appear. However, beam-rocking experiments usually involve a prolonged collection time, where the probe position is more or less shifted by an amount larger

than the unit-cell size owing to the specimen drift. As a result, the coherent interference effect should be smeared out, so that the beam convergence effect can be again considered as the incoherent superposition of partial incident plane-waves. Therefore, the beam convergence effect on X-ray ICPs can be assumed as the blurring of their contrast. It is thus recommended that a smaller convergence angle should be selected at a lower-order zone-axis orientation in which the ICP exhibits rather dense contrasts.

2.10 Extension of St-ALCHEMI

If there are a number of inequivalent sites for a host element in the unit cell and a doped impurity element occupies a part of those inequivalent sites, the St-ALCHEMI method is not applicable in its original form, because a single ICP can be obtained for the entire host element and one cannot assign the dopant ICP to the host ICPs from the different sites by their linear combination. The problem was examined by Rossouw *et al.* [44] for the Zn-doped $Mg_{12}(La_xCe_{1-x})$ lattice, where Zn was found to preferably occupy one of the three different Mg sublattice sites in a semi-quantitative manner, by comparing the experimental Zn ICP with theoretically calculated ICP for the three Mg sites. They assumed that the dopant ICP can be expressed by a linear combination of theoretically calculated ICPs of host elements, and the fractional distribution of the dopant over the possible sublattice sites was derived by minimizing the least-square fit. We treat the problem in a similar but more general way within the framework of St-ALCHEMI formulation, as follows.

If the theoretically calculated ICPs reproduce the experimental ICPs within the experimental accuracies (i.e., the noise level), the experimental site-specific ICPs of the host element, A can be obtained by the following proportional distribution scheme of the experimental ICP of element A, $I_{\mathrm{A}}(\mathbf{k}_i)$:

$$I_{\mathrm{A}(j)}(\mathbf{k}_i) = \frac{I^{\mathrm{Cal}}_{\mathrm{A}(j)}(\mathbf{k}_i)}{\sum_j I^{\mathrm{Cal}}_{\mathrm{A}(j)}(\mathbf{k}_i)} (I_{\mathrm{A}}(\mathbf{k}_i) - \Delta_{\mathrm{Bkg}}), \qquad (38)$$

where $I^{\mathrm{Cal}}_{\mathrm{A}(j)}(\mathbf{k}_i)$ is the calculated ICP of element A that is separately obtained for the individual *j*-th site. The actual theoretical calculations do not account for the Δ_{Bkg} contribution, although the Δ_{Bkg} contribution will be automatically incorporated again by the constant offset β in Eq. (31) in the multivariate linear regression procedure. Here, Δ_{Bkg} is estimated by the linear least-squares fitting in the following form:

$$\begin{bmatrix} I_{\mathrm{A}}(\mathbf{k}_1) \\ I_{\mathrm{A}}(\mathbf{k}_2) \\ \vdots \end{bmatrix} = C \cdot \begin{bmatrix} I^{\mathrm{Cal}}_{\mathrm{A}}(\mathbf{k}_1) \\ I^{\mathrm{Cal}}_{\mathrm{A}}(\mathbf{k}_2) \\ \vdots \end{bmatrix} + \Delta_{\mathrm{Bkg}} \cdot \begin{bmatrix} 1 \\ 1 \\ \vdots \end{bmatrix}, \qquad (39)$$

where the scaling factor C takes into account factors such as the incident electron beam current, the X-ray recording time per pixel, the X-ray fluorescence yield, and the detection efficiency.

Once the experimental ICPs from the inequivalent host sites are known, the original st-ALCHEMI method is applicable to specify the dopant occupation sites and their occupancies. It is noted that the crystal structure of the host lattice should be precisely known in advance. The application to a practical material is presented in section 3.2.

The above-extended version of ALCHEMI is not useful for the case where the atomic species under investigation is located on interstitial sites. This situation was already discussed by Rossouw *et al.* [45, 46], where the ICP of an interstitial species can be theoretically calculated to compare with the experimental ICP. They found that ICP analysis is more robust than Rietveld refinement of diffraction data [47] and convergent beam electron diffraction analysis, in that it does not require a highly accurate model of the host lattice framework and composition.

2.11 Accuracy evaluation based on statistical information extraction theories

In the extended St-ALCHEMI method where the dopant occupies multiple host sites, it is assumed that the ICPs from the different host sites are significantly different to one another. In other words, the vectors $I_{A(j)}^{\mathrm{Cal}}(\mathbf{k}_i)$ and $I_{A(j)}^{\mathrm{Cal}}(\mathbf{k}_j)$ $(i \neq j)$ are far enough from the parallel condition or linearly independent, otherwise it could be rather difficult to assign the dopant ICP to those from the different host sites with sufficient accuracy.

Here, the following two parameters are introduced in order to verify the statistical validity: the variance inflation factor (VIF) [48] and the *p*-value [49]. We briefly describe them below but please consult the corresponding references for more detail.

The VIF is an indicator for evaluating the degree of multi-collinearity between the basis vectors (i.e., predictor variables) in a least-squares regression analysis. The VIF for the *j*-th component, VIF_j, can be calculated by the formula:

$$VIF_j = \frac{1}{1 - R_j^2}, \tag{40}$$

where R_j^2 is the coefficient of determination [46] in which R_j^2 is nearly unity if the *j*-th basis vector is expressed by a linear combination of other components. The rule of thumb is that if the VIF > 10, the multi-collinearity is high, which means that the basis vector is significantly correlated with other predictor variables, and is therefore not linearly independent. However, if the VIF is well below 10, the basis vector is safely said to be linearly independent of the other basis vectors.

Another significance probability, frequently referred to as the *p*-value [49], is an indicator of the statistical reliability of the estimated regression coefficient. The *p*-value is the probability that a regression coefficient accidentally coincides with the statistically estimated value; the smaller the *p*-value is, the more probable it is that the regression coefficients actually have the estimated values. The rule of thumb is that if the *p*-value is less than 5%, then the regression coefficient is considered to be statistically reliable. In the general case of least-squares regression, the value of the regression coefficient α is obtained based on the central limit theorem, assuming a Gaussian probability distribution. If α is estimated from a finite number of sampling points, the standard deviation of the Gaussian probability distribution is in general unknown *a priori*. However, σ, the standard error of the estimated α, can be calculated. It is well-known that *t*-statics (calculated by the formula $t = (\alpha - \alpha_0) / \sigma$) follows the Student's *t*-distribution $f(t)$ [50]. The *p*-value is the cumulative probability that *t* takes a value greater than or equal to $|\alpha / \sigma|$, and is calculated according to the following formula:

$$p = \int_{\alpha/\sigma}^{\infty} f(t)\,dt + \int_{-\infty}^{-\alpha/\sigma} f(t)\,dt \quad . \qquad (41)$$

If t ($= \alpha / \sigma$) is located outside of the typical 95% confidence range of the *t*-distribution, the *p*-value is less than 5%. In such a case, the possibility that $\alpha = \alpha_0 = 0$ is significantly low, which means that the null hypothesis can be ruled out, and that the regression coefficient obtained is statistically significant.

3. Results and discussion

3.1 St-ALCHEMI in multi-dopant case [51, 52]

Eu^{3+}-doped Ca_2SnO_4 exhibits strong photoluminescence (PL) derived from the $^5D_0$–$^7F_2$ electric dipole transition of Eu^{3+} ions. Eu^{3+} had been regarded as being doped only at the Ca site of Ca_2SnO_4, where Ca vacancies were proposed to maintain charge balance. When only considering ionic radii, it is logical to assume that the Eu^{3+} (whose ionic radii are 1.01 Å and 0.95 Å when 7- and 6-coordinated with oxygen [53]) is incorporated onto the Ca^{2+} sites (1.06 Å [49]) because Eu^{3+} is much closer in size to Ca^{2+} than to Sn^{4+} (0.69 Å [53]). However, solid-state reaction synthesis and Rietveld analysis of powder X-ray diffraction (XRD) data by Yamane *et al.* revealed that Eu^{3+} equally occupies both the Ca^{2+} and Sn^{4+} sites [54]. The same group also prepared a Eu and Y co-doped sample $Ca_{1.8}Y_{0.2}Eu_{0.2}Sn_{0.8}O_4$, based on the idea that Y^{3+} ions with a smaller ionic radius preferentially occupy smaller cation (Sn^{4+}) sites, driving larger Eu^{3+} ions out of the Sn^{4+} site into the larger Ca^{2+} site [54]. $Ca_{1.8}Y_{0.2}Eu_{0.2}Sn_{0.8}O_4$ exhibited a stronger PL intensity than the Eu-doped sample $Ca_{1.9}Eu_{0.2}Sn_{0.9}O_4$, both of which had the same

Eu content in the formulae. The stronger PL in the co-doped sample is explained by the increased fraction of Eu^{3+} ions occupying the Ca site, because the Ca site is coordinated by seven oxygen atoms, the asymmetric configuration of which enhances the electric dipole moment, compared with the symmetric six-coordinated Sn site, as shown in Fig. 12 [21]. XRD-Rietveld analysis confirmed that preferential Ca^{2+} site occupation by Eu^{3+} and Sn^{4+} site occupation by Y^{3+} provide a small GOF indicator of the Rietveld fit in the co-doped samples [3], although it is not possible to determine the fraction of Eu(Y) that actually occupies the Ca^{2+}(Sn^{4+}) site. In this respect, it is important to quantitatively determine the site occupancies of this series of materials.

A series of Eu and Y co-doped samples with various dopant concentrations were synthesized and the site occupancies were determined directly by St-ALCHEMI. Samples of nominal compositions of $Ca_{1.9}Eu_{0.2}Sn_{0.9}O_4$ and $Ca_{1.8}Eu_{0.2}Y_{0.2}Sn_{0.8}O_4$ hereafter referred to as Eu20 and Eu20Y20, respectively, were examined.

Figure 13 shows the ECP and the ICPs of Ca-K, Sn-L, O-K, Eu-L, and Y-L for the Eu20Y20 sample around the [100] zone as representative examples. Initially, it appeared that the Eu-L ICP is closer to the Ca-K ICP, while the Y-L ICP to Sn-L ICP. This suggests that Eu and Y occupation sites could be biased as expected. The coefficients α_{ix} (i = Ca, Sn, x = Eu, Y) derived using Eq.(32), the site occupancies f_{ix} (Eq.(33)) of the impurities, and the impurity concentrations c of all the samples are presented in Table 1.

In Eu20, Eu^{3+} equally occupies the Ca^{2+} and Sn^{4+} sites ensuring the charge neutrality condition, which is consistent with the results of XRD-Rietveld analysis. On the other hand, in the co-doped samples, Eu^{3+} and Y^{3+} occupied the Ca^{2+} and Sn^{4+} sites at fractions of approximately 7:3 and 4:6, respectively, without resulting in a complete bias for a single site by a single element, which maintained the charge neutrality condition within the present experimental accuracies. The f_{ix}'s of the co-doped samples are nearly independent of the dopant concentration.

3.2 Multi-host site case [55]

Magnetoplumbite (M)-type strontium hexagonal ferrite, $SrFe_{12}O_{19}$, is a hard magnetic material that possesses strong magneto-crystalline anisotropy (MCA). It has been recently demonstrated that the MCA can be drastically improved by substituting La and Co for the Sr and Fe sites, respectively, with an optimized chemical formula of $Sr_{0.8}La_{0.2}Fe_{11.4}Co_{0.2}O_{19}$ [56, 57]; the occupation sites of Co, in particular, are believed to be a key factor in improving the MCA. It is thus important to investigate the amount of Co that is actually substituted, and at

which Fe sites, in order to discover the guiding principles that may determine further MCA improvements.

M-type ferrite has a long-period structure along the *c*-axis that exhibits five crystallographically inequivalent sites for Fe; in terms of Wyckoff notation, these include 12k, 2a, and $4f_2$ as the octahedral sites, the $4f_1$ tetrahedral site, and the 2b bipyramidal site, as shown in Fig. 14 [21]. Conventional XRD is inapplicable for occupancy analysis in this case because of the close atomic numbers of Fe and Co, as well as the small amount of Co (i.e., less than 0.7 at.%). In a previous study [58], the occupation sites of Co were first determined by Rietveld analysis of neutron diffraction data, suggesting seven plausible candidate models, which are shown in Table 2. The most probable model among them was selected by comparing the extended X-ray absorption fine structure (EXAFS) analysis results; this approach yielded model #7, wherein Co primarily occupies the $4f_1$ and 12k sites. On the other hand, a different model has also been reported, wherein Co mainly occupies the $4f_2$ site [59].

Because the atomic planes, including the five crystallographically inequivalent Fe sites, are consecutively aligned in the stack of basal planes perpendicular to the *c*-axis of the $SrFe_{12}O_{19}$ unit cell, the Fe site-selectivity should be revealed most effectively by tilting the incident beam around the axis that is perpendicular to the *c*-axis, and along the plane that includes the *c*-axis. One direction that satisfies the condition above is the $[1\bar{1}0]$ zone axis. A TEM image of the measured area is shown in Fig. 15. Accordingly, the incident electron beam was rocked about the $[1\bar{1}0]$ zone axis in an angular range of approximately ±3º along the radial direction, and EDXS spectra of 256 × 256 pixels were collected using the spectrum imaging mode. Two-dimensional X-ray ICPs for Sr, La, Fe, Co, and O were reconstructed using the Sr-L, La-L, Fe-K, Co-K, and O-K line net intensities, respectively. The background (owing to Bremsstrahlung) was subtracted, and overlapping characteristic X-ray peaks such as the Fe-K_β line (7.1 keV) and the Co-K_α line (6.9 keV) were separated according to the method implemented in the NSS software [41,60]. The X-ray ICPs were smoothed by averaging each pixel intensity over the neighbouring region of 3 × 3 pixels, thereby improving the signal-to-noise ratio. Translations, small rotations, shear, and dilatational distortions of the experimental ECP, and X-ray ICPs caused by instrumental imperfections were corrected using the affine transform [44].

Assuming that the concentration of the doped Co is small relative to that of Fe, and that Co replaces the Fe sites alone, the Co-K line intensity I_{Co} can be approximated by the following linear combination of the Fe-K line intensities $I_{Fe(2a)}$, $I_{Fe(2b)}$, $I_{Fe(4f1)}$, $I_{Fe(4f2)}$, and $I_{Fe(12k)}$ from the host Fe atoms occupying the 2a, 2b, $4f_1$, $4f_2$, and 12k sites, respectively, according to Eq.(39) as:

$$\begin{bmatrix} I_{\mathrm{Co}}(\mathbf{k}_1) \\ I_{\mathrm{Co}}(\mathbf{k}_2) \\ \vdots \end{bmatrix} = \alpha_{2a}\begin{bmatrix} I_{\mathrm{Fe(2a)}}(\mathbf{k}_1) \\ I_{\mathrm{Fe(2a)}}(\mathbf{k}_2) \\ \vdots \end{bmatrix} + \alpha_{2b}\begin{bmatrix} I_{\mathrm{Fe(2b)}}(\mathbf{k}_1) \\ I_{\mathrm{Fe(2b)}}(\mathbf{k}_2) \\ \vdots \end{bmatrix} + \alpha_{4f_1}\begin{bmatrix} I_{\mathrm{Fe(4f_1)}}(\mathbf{k}_1) \\ I_{\mathrm{Fe(4f_1)}}(\mathbf{k}_2) \\ \vdots \end{bmatrix} + \alpha_{4f_2}\begin{bmatrix} I_{\mathrm{Fe(4f_2)}}(\mathbf{k}_1) \\ I_{\mathrm{Fe(4f_2)}}(\mathbf{k}_2) \\ \vdots \end{bmatrix} + \alpha_{12k}\begin{bmatrix} I_{\mathrm{Fe(12k)}}(\mathbf{k}_1) \\ I_{\mathrm{Fe(12k)}}(\mathbf{k}_2) \\ \vdots \end{bmatrix} + \beta\begin{bmatrix} 1 \\ 1 \\ \vdots \end{bmatrix}, \quad (42)$$

The coefficients α_j (in the present case, j = the 2a, 2b, $4f_1$, $4f_2$, and 12k sites) and β can be derived by a multivariate linear regression if the $\{I_{\mathrm{Fe}(j)}(\mathbf{k}_i)\}$ values are separately known. The constant offset β models the experimental relationship between the ICPs well, taking into account the errors in the background subtraction, the orientation-independent X-ray signals from Fe or Co (de-channelling effects) or surface amorphous effects, and the secondary fluorescent emission from the specimen or microscope column, as mentioned in section 2.6 [40]. By using the best-fit parameters, α_j, the Co concentration, c_{Co}, and the relative fraction of Co occupying the j-th site, $f^{j}{}_{\mathrm{Co}}$, can be quantified by Eq. (33), where $\Sigma_j f^{j}{}_{\mathrm{Co}}$ is assumed to be 1. c_{Fe} is the Fe concentration, and n_j is the fraction of Fe that occupies the j-th site. The Fe concentration and occupancies can be considered to be those of the non-doped sample to a good approximation because of the small Co concentration. k_{Fe} and k_{Co} are the k-factors of Fe and Co, respectively; their ratio $k_{\mathrm{Fe}}/k_{\mathrm{Co}}$ was obtained to be 0.99 using the database in the NSS software.

It should be noted here that the site-specific X-ray intensities, $I_{\mathrm{Fe}(j)}$, are not directly measured separately, and the extended St-ALCHEMI method introduced in section 2.10 is applied: if the theoretically calculated ICPs reproduce the experimental ICPs within the experimental accuracies (i.e., the noise level), the experimental site-specific ICPs of the host element can be obtained by Eq. (38), where $I_{(j)}{}^{\mathrm{Cal}}$ is the calculated ICP that is separately obtained for the individual j-th host element site. The actual theoretical calculations do not take the Δ_{Bkg} contribution into account, although the Δ_{Bkg} contribution will be automatically incorporated later by the constant offset β in Eq. (42) in the multivariate linear regression procedure. Here, Δ_{Bkg} is estimated by Eq. (39), where the scaling factor C takes into account factors such as the incident electron beam current, the X-ray recording time per pixel, the X-ray fluorescence yield, and the detection efficiency.

Simulations of characteristic X-ray emissions were performed based on dynamical electron diffraction theory described in section 2.5. Under the local approximation, which reasonably holds for the case of EDXS [26, 61], a simulated characteristic X-ray intensity $I_\kappa(\mathbf{k})$ can be expressed by a slightly modified form of Eq. (25):

$$I_\kappa(\mathbf{k}) = Q \cdot T \cdot D_\kappa \cdot \left(\frac{\Omega}{4\pi}\right) \cdot \omega_\kappa \int |\Psi(\mathbf{r},\mathbf{k})|^2 V_\kappa^{\mathrm{core}}(\mathbf{r}) X_\kappa^{\mathrm{abs}}(z)\, d\mathbf{r} \quad , \qquad (43)$$

where $\Psi(\mathbf{r}, \mathbf{k})$ is the incident electron wavefunction at position $\mathbf{r}$ within the crystal, and $V_\kappa^{\mathrm{core}}(\mathbf{r})$ is the effective transition potential for core excitation [34]. The fraction of generated X-rays that escape from the specimen is:

$$X_{\kappa}^{\mathrm{abs}}(z) = \exp(-R(z)\mu\rho), \tag{44}$$

where

$$R(z) = \frac{z\cos\theta}{\sin(\theta+\varphi)} \tag{45}$$

is the X-ray transmission path within the specimen for the detector take-off angle φ and the specimen-tilt angle θ. Lastly, μ and ρ are the X-ray mass absorption coefficient and the density, respectively [36].

In this study, $\Psi(\mathbf{r}, \mathbf{k})$ was calculated by the Bloch-wave approach, and thus the X-ray yield owing to the TDS electrons was estimated under the single inelastic scattering and kinematical approximations, in which TDS electrons take on the plane-wave form [22, 33, 35, 62]. The effects of Q, T, D_{κ}, $\Omega/4\pi$, and ω_{κ} were absorbed into the scaling factor C in the fit between the simulation and experimental data.

If the difference between the values of $X_{\kappa}^{\mathrm{abs}}(z)$ for Fe and Co is negligible owing to the neighbouring elements or the absorption effects not being taken into account, then we can assume that the term $|\Psi(\mathbf{r}, \mathbf{k})|^2 X_{\kappa}^{\mathrm{abs}}(z)$ in Eq. (43) is a common factor for both Fe and Co. From this point, the common factor can be cancelled out in the X-ray intensities in Eq. (42). Accordingly, the intensity ratio between the X-ray signals from Fe and Co can be expressed in the following manner:

$$\frac{I_{\mathrm{Fe}}}{I_{\mathrm{Co}}} = \frac{D_{\mathrm{Fe}}\omega_{\mathrm{Fe}} f_{\mathrm{Fe}}^{\mathrm{core}}(0) c_{\mathrm{Fe}}}{D_{\mathrm{Co}}\omega_{\mathrm{Co}} f_{\mathrm{Co}}^{\mathrm{core}}(0) c_{\mathrm{Co}}} = \frac{(1/k_{\mathrm{Fe}})c_{\mathrm{Fe}}}{(1/k_{\mathrm{Co}})c_{\mathrm{Co}}} = \frac{k_{\mathrm{Co}}}{k_{\mathrm{Fe}}} \cdot \frac{c_{\mathrm{Fe}}}{c_{\mathrm{Co}}}, \tag{46}$$

where $f_{\mathrm{Fe}}^{\mathrm{core}}(0)$ and $f_{\mathrm{Co}}^{\mathrm{core}}(0)$ are the ionization cross-sections ($f_{\kappa}^{\mathrm{core}}(s = 0)$: atomic scattering factor for ionization [33]) for the isolated Fe and Co atoms, respectively. In this way, the ratio $k_{\mathrm{Fe}}/k_{\mathrm{Co}}$ turns out to be unity according to the tabulated $f_{\kappa}^{\mathrm{core}}$ [34] and ω_{κ} [63] values, assuming that $D_{\mathrm{Fe}} \approx D_{\mathrm{Co}}$.

A bright-field TEM image and the corresponding electron diffraction pattern of the crystal grain used for the beam-rocking EDXS experiment are shown in Figs. 15(a) and (b), respectively. The sample thickness at the illuminated area was estimated to be approximately 120 nm from the low-loss EELS spectrum, and the measured value was cross-checked by the estimation using the convergent-beam electron diffraction (CBED) pattern [31, 64].

ECP and X-ray ICPs for the Fe-K, Sr-L, O-K, Co-K, and La-L lines after correcting for the geometrical distortions are shown in Fig. 16. It should be particularly noted that a wide bright band is observed in the Fe-K ICP along the [110] direction passing through the centre, whereas the Co-K ICP exhibits the splitting narrow bright bands in the same area. This implies that Co preferentially occupies parts of the inequivalent Fe sites, as opposed to the case of a uniform

substitution. On the other hand, the La-L ICP is very similar to the Sr-L ICP, suggesting that La occupies the Sr site alone.

The experimental Fe-K ICP was compared with the theoretical Fe-K ICP, which was calculated for non-doped $SrFe_{12}O_{19}$ owing to the small concentration of impurities; this is shown in Figs. 17(a) and (b), where the scaling parameter, C, and the offset, Δ_{Bkg}, were optimized to show the best fit between the two. Their intensity profiles along the $[00\bar{1}]$ direction, projected to the [110] direction, are also shown in Fig. 17(c) for better comparison. The experimental and theoretical results exhibit good agreement with each other, although slight asymmetric discrepancies are observed on the right side of Fig. 17(c). However, such discrepancies can always occur, presumably because the pivot point of the rocking beam wanders on the sample areas with slightly different thicknesses because of imperfect beam alignment and/or lens aberrations. Nevertheless, this exerts little influence on the final quantitative results, because we have theoretically confirmed that the intensity ratio of X-rays emitted from individual Fe sites is not drastically affected by this degree of thickness fluctuation.

The site-specific Fe-K ICPs for the 2a, 2b, $4f_1$, $4f_2$, and 12k sites were then extracted by applying Eq. (38), as shown in the upper row of Fig. 18, together with the corresponding theoretically calculated ICPs below each decomposed ICP. It should be noted that split bright bands are seen in the decomposed Fe(2a)-K and Fe($4f_1$)-K ICPs, just as in the experimental Co-K ICP, which suggests preferential Co-occupation on the 2a and $4f_1$ sites. The VIF values described in section 2.11 for these site-specific ICPs were calculated to be 4.5, 1.4, 5.6, 2.8, and 3.4 for the 2a, 2b, $4f_1$, $4f_2$, and 12k sites, respectively; this is well below the threshold of 10, thereby confirming that the site-specific ICPs are hardly correlated with one another in a multi-co-linear manner. Accordingly, we do not have to anticipate rank deficiency in the following multivariate liner regression.

The St-ALCHEMI method was then applied for quantitative analysis of the dataset consisting of the decomposed Fe-K ICPs for the five Fe sites and the Co-K ICP. The fitted coefficients α_j, produced by the multivariate linear regression based on Eq. (46), are listed in Table 3. All of their p-values were estimated to be less than 2%, which falls well below the 5% threshold, thereby indicating that the obtained α_j values are statistically reliable. The experimental Co-K ICP reproduced from Fig. 16 and the fitted Co-K ICP (according to the formula, $\Sigma_j \alpha_j I_{Fe(j)} + \beta$) are shown in Figs. 19(a) and (b), respectively. The residual image, $I_{Co} - \Sigma_j \alpha_j I_{Fe(j)} - \beta$, is presented in Fig. 19(c), which shows no appreciable structures. In fact, the intensity distribution is almost the same as the estimated experimental noise extracted by a high-pass filter from the Co-K ICP. To show this in a more quantitative manner, the intensity

distributions of the residual image and the estimated experimental noise image (upper-right corner) are shown in Fig. 19(d). The standard deviations of the residual image, σ_{res}, and of the noise image, σ_{noise}, result in a ratio of $\sigma_{res}/\sigma_{noise}$ = 0.8, which means that the fitted Co-K ICP agrees with the experimental Co-K ICP within the experimental accuracy (i.e., the noise level). It should be noted that these regression results were reproduced, within the experimental accuracy, using different experimental datasets obtained from the same crystal grain. Furthermore, measurements using different crystal grains (i.e., grains located at different observation areas) also showed similar results.

The occupancies of Co to the five Fe sites, along with the associated concentrations, are listed in Table 3 by using the obtained α_j values and Eqs. (33)-(35) for k_{Fe}/k_{Co} values extracted from the NSS software and the other as calculated theoretically [63]. It should be noted that the difference in the *k*-factor ratio, k_{Fe}/k_{Co}, propagates to the differences in the final f_{Co}^{j} and c_{Co} values within the same (or smaller) order of magnitude. The results of the present analysis suggest that Co preferentially occupies the 2a, $4f_1$, and 12k sites. This tendency is consistent with the most plausible model (i.e., #7) listed in Table 2, which was estimated by the combined neutron diffraction/Rietveld analysis and the EXAFS analysis [58].

In conclusion, the occupation sites of Co, which are key parameters for improving the MCA, were determined to be the 2a, $4f_1$, and 12k sites, which is consistent with the results of the previous neutron diffraction/EXAFS analysis. The result is also consistent with the energetics considerations provided by first-principles calculations [55].

3.3 Concurrent HARECXS/HARECES

Ni-substituted lithium manganese oxide spinel ($LiNi_xMn_{2-x}O_4$, space group: *Fd*-3*m*) is one of the most promising positive electrode materials for rechargeable lithium ion batteries, because of its high operating voltage and low toxicity and cost. $LiNi_xMn_{2-x}O_4$ is considered to have an *fcc* framework of oxygen ions, with lithium ions occupying the tetrahedral (8a) sites, and manganese and nickel ions situated at the octahedral (16d) sites. However, XRD measurements of $LiNi_xMn_{2-x}O_4$ synthesized by a particular reaction path revealed that some of the nickel ions occupied the tetrahedral rather than the octahedral sites [65]. The quantitative analysis using this method remains controversial, however, because XRD analysis could be insensitive to the degree of cation mixing, particularly for multi-doped transition metal (TM) elements owing to their close atomic numbers. Neutron diffraction is a more reliable method for such cases, though it is neither easy to use nor applicable to samples smaller than 1 μm. In this context, the HARECXS/HARECES methods can be promising alternatives.

It is generally believed that Mn in $LiNi_xMn_{2-x}O_4$ can be trivalent or tetravalent, depending on the amount of Ni-substitution and/or the loss of oxygen [65–68], whereas Ni remains divalent [65, 68]. Although conventional EELS and XPS measurements have been adopted to investigate the valence states of cations, these techniques only provide information averaged over atoms at different sites. Hence, we determined the relationship between the site occupancy and the valence state of the cations in $LiNi_xMn_{2-x}O_4$ [69]. The present section aims to clarify this relationship in a deliberately and excessively Ni-doped sample material (determined as $Li_{0.21}Ni_{0.7}Mn_{1.64}O_{4-\delta}$) by the combined HARECXS and HARECES analysis [70].

In previous studies [15,17–19], the matrix equation (12) has been solved by applying the MCR technique for materials with known site occupancies (N_{site}). In the present study, however, the HARECXS data simultaneously measured with HARECES directly provides the N_{site} values. To relate the site occupancies to the elements in the matrix **C**, the total core-loss cross-section for each site, σ_{site}, in the present experimental geometry is needed. σ_{site} is obtained by integrating the second-order differential Eqs. (16)–(19) for a specimen with thickness t. In case of small $\boldsymbol{q}$ and $\boldsymbol{q}'$—typically less than 1.0|**g**| [19]—the MDFF can be expressed by the simple inner product of $\boldsymbol{q}$ and $\boldsymbol{q}'$ within the dipole transition approximation [30]. Each element C_{site} in **C** is consequently expressed by the following normalized weight coefficient at each diffraction condition (tilting angle of the incident beam):

$$C_{tet} = \frac{N_{tet}\sigma_{tet}}{N_{tet}\sigma_{tet} + N_{oct}\sigma_{oct}}. \qquad (47)$$

Because the **C** matrices can be estimated by the theoretical site-specific inelastic scattering cross-sections and experimental N_{site} using HARECXS, Eq. (12) can be solved by simply applying a multivariate linear regression to extract the component spectra of the TM at the tetrahedral and octahedral sites.

HARECXS measurements were performed by tilting the incident beam with a systematic excitation of, for instance, −4**g** to 4**g**, where **g** = 4 0 0. Data of the characteristic X-rays up to 20 keV were acquired, with recording times of 10–50 s per tilt angle. The O-, Mn-, and Ni-K_α line intensities were extracted from the dataset.

A series of the Mn-L_3 ELNES with the incident beam subsequently tilted under the condition with the 400 systematic row of reflections excited, and the Mn-K_α HARECXS rocking curves taken at the same time are shown in Fig. 20(a) and (b), respectively. Each HARECES curve in Fig. 20(a) is displaced along the vertical axis so that its baseline position corresponds to the position of the vertical axis in Fig. 20(b). It is seen in Fig. 20(a) that the peak near 639 eV (fingerprint of Mn^{2+}) is enhanced for $1 \le k_x/|\mathbf{g}| \le 2$, where the atomic planes including the

tetrahedral sites are preferentially excited. On the other hand, the peak near 642 eV (fingerprint of Mn^{4+}) is dominant for $0 \leq k_x/|\mathbf{g}| \leq 1$, where the octahedral sites are preferentially excited. This tendency is the qualitative evidence for the correlation between the site occupancy and valence state of the manganese ion. The HARECXS profile of the Mn-*K* is best fitted by the linear combination of Mn_{oct} and Mn_{tet} profiles with a ratio of 63:37. The Mn-L_3 ELNES selectively obtained for the tetrahedral and octahedral sites, were extracted by solving Eq. (12) and are shown in Fig. 21, together with the reference divalent, trivalent, and tetravalent Mn-L_3 spectra. All the spectra were normalized by the respective integrated spectral intensities. The **C** matrix was prepared according to Eqs. (12) and (47) by the site occupancies derived from the HARECXS data (as discussed in section 2.3) and the theoretical site-specific total cross-sections using the analytical formula in the two-beam approximation (Eq. (11) in ref. [15]), because the simulation results by the two-beam approximation and the fully dynamical many-beam calculation code [32] showed little difference in the range of $0.5 \leq k_x/|\mathbf{g}| \leq 1.5$. The spectral profile of Mn_{oct}-L_3 is in good agreement with that of Mn^{4+}, suggesting that the Mn ions at the octahedral sites are essentially tetravalent. On the other hand, the spectral profile of Mn_{tet}-L_3 is similar to that of Mn^{2+}, indicating that most of the Mn ions at the tetrahedral sites are divalent, with possibly a slight amount of other valence states. This reduced valence state is consistent with the oxygen deficiency of this sample compared to the other samples, judging from the lower relative intensity ratio of O-*K*/Mn-$L_{2,3}$. The net cation charge is significantly less than 8, which is attributable to its observed oxygen deficiency.

4. Summary and future prospects

In this article, we outlined the current development of element/site-selective microanalysis for quantitatively estimating the site occupancies of impurities and their chemical states, using electron channelling under incident electron beam rocking conditions. The present method is applicable to a wide range of materials where other conventional diffraction techniques such as X-ray or neutron diffraction combined with Rietveld analysis fail because of limited sample sizes, close scattering-factors of neighbouring elements in the periodic table, or multiple possible atomic sites. In particular, the direct X-ray channeling pattern reliably extracts information from a minority species. This contrasts with the inability to isolate individual atomic responses by Rietveld analysis. It is anticipated that the core levels of light elements may be delocalized, which can give rise to insufficient electron channelling effects to facilitate site determination. As seen in Figs. 8, 13, and 16, oxygen exhibits unambiguous channelling

patterns and we must further examine if the present schemes are applicable to other light elements.

Considering that the ICPs can be precisely predicted by theoretical simulation, the method can be extended to detect the displacements and vacancy concentrations of host elements, in addition to the ordering of dopants along the specific types of grain boundaries of oxide ceramics. These applications should offer a good alternative technique applicable to relatively thick samples, because typical column-by-column analysis using atomic-resolution aberration-corrected STEM requires the preparation of a very thin sample that is free from surface amorphous damage layers. As described in the Introduction, an electron beam that is incident along the low-order zone axis can spread over the neighbouring atomic columns owing to the electron channelling effects, which significantly hampers quantitative analysis unless the sample thickness is generally less than 20 nm. In addition, the present method would be applicable to samples with surface amorphous damage layers. It is also anticipated that physical properties of such ultra-thin samples can be modified from their native states during the thinning process.

The beam rocking mode in the ASID window (in JEOL STEMs) allows us at present to focus the beam down to a minimum of ~300 nm, using the smallest condenser aperture, which limits the convergence angle of the incident beam and causes difficulties with the pivot point. We aim to reduce the minimum measurable area down to ~100 nm or less, while maintaining a convergence angle of less than 5 mrad to further extend application capabilities to more localized areas. In addition, the parameters for calculating the ionization cross-sections using tabulated inelastic-scattering factors are available up to Z = 60 (Nd) [34]. We are now attempting to extend the database to heavier elements, including several rare earth elements that are important for applications.

The St-ALCHEMI method and its extension are applicable to cases where the material of interest is crystalline with a known structure. We are now further extending the methods in order to tolerate these limitations to systems containing lattice defects such as grain boundaries or small atomic displacements associated with ordered vacancies.

Acknowledgments

This work is in part supported by Grants-in-Aid for Scientific Research on Innovative Areas "Nano Informatics" (No. 25106004), Kiban-kenkyu A (No. 26249096), and Wakate-kenkyu B (No. 26870271) from the Japan Society of the Promotion of Science.

References

[1] D. J. Singh, Planewaves, Pseudopotentials and the LAPW Method, Kluwer Academic, Dordrechit, 1994.

[2] H. M. Rietveld, A profile refinement method for nuclear and magnetic structures, J. Appl. Crystallogr. 2 (1969) 65–71.

[3] F. Izumi, T. Ikeda, A Rietveld-analysis program RIETAN-98 and its applications to zeolites, Mater. Sci. Forum. 321–324 (2000) 198–203.

[4] H. H. Rose, Optics of high-performance electron Microscopes, Science and Technology of Adv. Mater. 9 (2008) 014107.

[5] D. A. Muller, L. Fitting Kourkoutis, M. Murfitt, J. H. Song, H. Y. Hwang, J. Silcox, N. Dellbyand, O. L. Krivanek, Atomic-Scale Chemical Imaging of Composition and Bonding by Aberration-Corrected Microscopy, Science 319 (2008) 1073-1076.

[6] N. R. Lugg, G. Kothleitner, N. Shibata, Y. Ikuhara, On the quantitativeness of EDS STEM, Ultramicrosc. 151 (2015) 150–159.

[7] P. B. Hirsch, A. Howie, R. B. Nicholson, D.W. Pashley, M. J. Whelan, Electron Microscopy of Thin Crystals, Krieger, Florida, 1977.

[8] J. C. H. Spence, J. Taftø, ALCHEMI: a new technique for locating atoms in small crystals, J. Microsc. 130 (1982) 147-154.

[9] J. Taftø, J. C. H. Spence, Crystal site location of iron and trace elements in an Mg-Fe olivine using a new crystallographic technique, Science 218 (1982) 49-51.

[10] S. Matsumura, T. Soeda, N. J. Zaluzec, C. Kinoshita, Electron Channeling X-ray Microanalysis for Cation Configuration in Irradiated Magnesium Aluminate Spinel, Mater. Res. Soc. Proc. 589 (1999) 129-134.

[11] K. Yasuda, T. Yamamoto, S. Matsumura, The atomic structure of disordered ion tracks in magnesium aluminate spinel, J. Microsc. 59 (2007) 27.

[12] N. J. Zaluzec, Measurement of Crystal Symmetry using HARECXS, Microsc. Microanal. 11 (Suppl. 2) (2005) 720-721

[13] N. J. Zaluzec, High Angular Resolution Channeling X-ray/Electron Spectroscopy, Microsc. Microanal. 18 (Suppl. 2) (2012) 678-679.

[14] J. Taftø, O. L. Krivanek, Site-specific valence determination by electron energy-loss spectroscopy, Phys. Rev. Lett. 48 (1982) 560-563.

[15] K. Tatsumi, S. Muto, Local electronic structure analysis by site-selective ELNES using electron channeling and first-principles calculations, J. Phys.: Condens. Mat. 21 (2009) 104213-1-14.

[16] S. Muto, T. Yoshida, K. Tatsumi, Diagnostic nano-analysis of materials properties by multivariate curve resolution applied to spectrum images by S/TEM-EELS, Mater. Trans. 50 (2009) 964-969.

[17] Y. Yamamoto, K. Tatsumi, S. Muto, Site-Selective Electronic Structure of Aluminum in Oxide Ceramics Obtained by TEM-EELS Analysis Using the Electron Standing-Wave Method, Mater. Trans. 48 (2007) 2590-2594.

[18] K. Tatsumi, S. Muto, I. Nishida, J. Rusz, Site-specific electronic configurations of Fe 3d states by energe loss by channeled electrons, Appl. Phys. Lett. 96 (2010) 201911.

[19] K. Tatsumi, S. Muto, J. Rusz, Energy Loss by Channeled Electrons: A Quantitative Study on Transition Metal Oxides, Microscopy and microanalysis. 19 (2013) 1586-1594.

[20] S. J. Pennycook, J. Narayan, Atom Location by Axial-Electron-Channeling Analysis, Phys. Rev. Lett. 54 (1985) 1543-1546.

[21] K. Momma and F. Izumi, VESTA 3 for three-dimensional visualization of crystal, volumetric and morphology data, J. Appl. Crystallogr. 44 (2011) 1272-1276.

[22] M. P. Oxley, L. J. Allen, ICSC: a program for calculating inelastic scattering cross sections for fast electrons incident on crystals, J. Appl. Cryst. 36 (2003) 940-943.

[23] J. H. Wang, P. K. Hopke, T. M. Hancewicz, S. L. Zang, Application of modified alternating least squares regression to spectroscopic image analysis, Anal. Chim. Acta. 476 (2003) 93–109.

[24] D. D. Lee, H. S. Seung, Algorithms for non-negative matrix factorization, Adv. Neural Inform. Process. Syst. 13 (2001) 556–562.

[25] H. Yoshioka, Effect of Inelastic Waves on Electron Diffraction, J. Phys. Soc. Jpn. 12 (1957) 618-628.

[26] L. J. Allen, A. J. D'Alfonso, S. D. Findlay, Modelling the inelastic scattering of fast electrons, Ultramicrosc. 151 (2015) 11–22.

[27] L. V. Hove, Correlation in Space and Time and Born Approximation Scattering in Systems of interacting Particles, Phys. Rev. 95 (1955) 249

[28] H. Kohl, H. Rose, Theory of image-formation by inelastically scattered electrons in the electron-microscope, Advances in Electronics and Electron Physics. 65 (1985) 173-227.

[29] P. Schattschneider, *Fundamentals of Inelastic Electron Scattering*, Springer, Wien, 1986.

[30] P. Schattschneider, M. Nelhiebel, M. Schenner, W. Grogger, F. Hoffer, Diffraction effects in inner-shell ionization edges, J. Microsc. 183 (1996) 18-26.

[31] J. C. H. Spence, J. M. Zuo, *Electron Microdiffraction*, Plenum Press, New York, 1992.

[32] J. Rusz, S. Muto, K. Tatsumi, New algorithm for efficient Bloch-waves calculations of orientation-sensitive ELNES, Ultramicrosc. 125 (2013) 81-88.

[33] M. P. Oxley, L. J. Allen, Delocalization of the effective interaction for inner-shell ionization in crystals, Phys. Rev. B. 57 (1998) 3273-3282.

[34] M. P. Oxley, L. J. Allen, Atomic scattering factors for K-shell and L-shell ionization by fast electrons, Acta Cryst. A56 (2000) 470–490.

[35] L. J. Allen, T. W. Josefsson, Inelastic scattering of fast electrons by crystals, Phys. Rev. B. 52 (1995) 3184–3198.

[36] C. J. Rossouw, C. T. Forwood, M. A. Gibson, P. R. Miller, Generation and absorption of characteristic X-rays under dynamical electron diffraction conditions, Micron 28 (1997) 125–137.

[37] C. J. Rossouw, P. S. Turner, T. J. White, A. J. O'Connor, Statistical analysis of electron channelling microanalytical data for the determination of site occupancies of impurities, Philos. Mag. Lett. 60 (1989) 225–232.

[38] P. S. Turner, T. J. White, A. J. O'Connor, C. J. Rossouw, Advances in ALCHEMI analysis, J. Microsc. 162 (1991) 369–378.

[39] T. W. Josefsson, L. J. Allen, P. R. Miller, C. J. Rossouw, *K*-shell ionization under zone-axis electron-diffraction conditions, Phys. Rev. B. 50 (1994) 6673.

[40] M. P. Oxley, L. J. Allen, C. J. Rossouw, Correction terms and approximations for atom location by channelling enhanced microanalysis, Ultramicrosc. 80 (1999) 109–124.

[41] J. J. McCarthy, F. H. Schamber, Least-squares fit with digital filter, a status report, National Bureau of Standards Special Publication 604: Proceeding of the Workshop on Energy Dispersive X-Ray Spectroscopy, (1979) 273–296.

[42] C. T. Koch, Aberration-compensated large-angle rocking beam electron diffraction, Ultramicrosc. 111 (2011) 828-840.

[43] Dr Chris Boothroyd: TIA (Emispec) file format, http://www.er-c.org/cbb/info/TIAformat/

[44] C. J. Rossouw, C. J. Bettles, T. J. Davis, C. T. Forwood, P. R. Miller, K. Venkatesan, Location of Zn within the $Mg_{12}(La_xCe_{1-x})$ lattice by X-ray incoherent channelling patterns, Acta Cryst. A57 (2001) 321–332.

[45] C. J. Rossouw and P. R. Miller, Location of interstitial Cr in mullite by incoherent channelling patterns from characteristic X-ray emission, Amer. Mineral. 84 (1999) 965-969.

[46] C. J. Rossouw and P. R. Miller, Analysis of incoherent channelling patterns formed by X-ray emission from host lattice species and interstitial Cr in mullite, J. Electron Microscopy 48 (1999) 849-864.

[47] R. X. Fischer and H. Schneider, Crystal structure of Cr-mullite, Amer. Mineral. 85 (2000) 1175-1179.

[48] M. H. Kutner, C. J. Nachtsheim, J. Neter, Applied Linear Regression Models, McGraw-Hill/Irwin, New York, 2004.

[49] R. Nuzzo, Scientific method: Statistical errors, Nature 506 (2014) 150–152.

[50] T. O. Kvalseth, Cautionary Note about R^2, Am. Stat. 39 (1985) 279–285.

[51] Y. Fujimichi, S. Muto, K. Tatsumi, T. Kawano, H. Yamane, Quantitative determination of site occupancy of multi-rare-earth elements doped into Ca_2SnO_4 phosphor by electron channeling microanalysis, J. Solid State Chem. 183 (2010) 2127-2132.

[52] S. Muto, Y. Fujimichi, K. Tatsumi, H. Yamane and T. Kawano, Site occupancy determination of Eu/Y doped in Ca_2SnO_4 phosphor by electron channeling microanalysis, Optical Mater. 33 (2011) 1015-1018.

[53] L. Jiang, C. Chang, D. Mao, C. Feng, Concentration quenching of Eu^{2+} in $Ca_2MgSi_2O_7$:Eu^{2+} phosphor, Mater. Sci. Eng. B. 103 (2003) 271-275.

[54] H. Yamane, T. Yamada, T. Kawano, Mater. Integ. 22 (2009) 6-11.

[55] M. Ohtsuka, S. Muto, K. Tatsumi, Y. Kobayashi, T. Kawata, Quantitative determination of occupation sites trace Co substituted for multiple Fe sites in M-type hexagonal ferrite using statistical beam-rocking TEM-EDXS analysis, Microscopy 65 (2016) 127-137.

[56] K. Iida, Y. Minachi, K. Masuzawa, M. Kawakami, H. Nishio, H. Taguchi, M-type Sr-Ferrite Containing Lanthanum and Cobalt, J. Magn. Soc. Jan. 23 (1999) 1093–1096.

[57] Y. Ogata, T. Takami, Y. Kubota, Development of La-Co Substituted Ferrite Magnets, J. Jpn. Soc. Powder Metall. 50 (2003) 636–641.

[58] Y. Kobayashi, E. Oda, T. Nishiuchi, T. Nakagawa, Cation distribution analysis of Sr–La–Co M-type ferrites by neutron diffraction, extended X-ray absorption fine structure and X-ray magnetic circular dichroism, J. Ceramic Soc. Jpn. 119 (2011) 285–290.

[59] J. M. Le Breton, J. Teillet, G. Wiesinger, A. Morel, F. Kools, P. Tenaud, Mössbauer investigation of Sr-Fe-O hexaferrites with La-Co addition, IEEE Trans. Magn. 38 (2002) 2952–2954.

[60] D. J. McMillan, G. D. Baughman, F. H. Schamber, Experience with multiple-least-squares fitting with derivative references, Microbeam Analysis 1985, (1985) 137–140.

[61] Z. Chen, A. J. D'Alfonso, M. Weyland, D. J. Taplin, L. J. Allen, S. D. Findlay, Energy dispersive X-ray analysis on an absolute scale in scanning transmission electron microscopy, Ultramicrosc. 157 (2015) 21–26.

[62] M. Ohtsuka, S. Muto, Slice-by-slice simulations of absorption potential for high-angular resolution electron channeled X-ray spectroscopy, Proc. of 18th Inter'l Microsc. Cong. (2014)1243–1244.

[63] J. H. Hubbell, P. N. Trehan, N. Singh, B. Chand, D. Mehta, M. L. Garg, R. R. Garg, S. Singh, S. Puri, A Review, Bibliography, and Tabulation of K, L, and Higher Atomic Shell X-Ray Fluorescence Yields, J. Phys. Chem. Ref. Data. 23 (1994) 339–364.

[64] J. M. LeBeau, S. D. Findlay, L. J. Allen, S. Stemmer, Position averaged convergent beam electron diffraction: Theory and applications, Ultramicrosc. 110 (2010) 118–125.

[65] Y. Wei, K. B. Kim, G. Chen, Evolution of the local structure and electrochemical properties of spinel $LiNi_xMn_{2-x}O_4$ ($0 \leq x \leq 0.5$), Electrochim. Acta 51 (2006) 3365–3373.

[66] Q. Zhong, A. Bonakdarpour, M. Zhang, Y. Gao, J. R. Dahn, Synthesis and electrochemistry of $LiNi_xMn_{2-x}O_4$, J. Electrochem. Soc. 144 (1997) 205–213.

[67] J. H. Kim, S. T. Myung, C. S. Yoon, S. G. Kang, Y. K. Sun, Comparative study of $LiNi_{0.5}Mn_{1.5}O_{4-\delta}$ and $LiNi_{0.5}Mn_{1.5}O_4$ cathodes having two crystallographic structures: $Fd\bar{3}m$ and $P4_332$, Chem. Mater. 16 (2004) 906–914.

[68] L. W. Ma, B. Z. Chen, X. C. Shi, W. Zhang, K. Zhang, Stability and Li^+ extraction/absorption properties of $LiM_xMn_{2-x}O_4$ (M = Ni, Al, Ti; $0 \leq x \leq 1$) in aqueous solution, Colloids and Surfaces A 369 (2010) 88–94.

[69] K. Amine, H. Tukamoto, H. Yasuda, Y. Fujita, Preparation and electrochemical investigation of $LiMn_{2-x}Me_xO_4$ (Me: Ni, Fe, and x = 0.5, 1) cathode materials for secondary lithium batteries, J. Power Sources 68 (1997) 604–608.

[70] Y. Yamamoto, K. Kataoka, J. Akimoto, K. Tatsumi, T. Kousaka, J. Ohnishi, T. Takahashi, S. Muto, Quantitative analysis of cation mixing and local valence states in $LiNi_xMn_{2-x}O_4$ using concurrent HARECXS and HARECES measurements, Microscopy 65 (2016) 253-262.

Figure captions

Figure 1 Schematic diagrams of the two types of Bloch wave intensity distributions at the reflecting position in a simple cubic lattice in the direction normal to the reflecting planes. The electron current flow is parallel to the reflecting planes.

Figure 2 Dispersion surface in the two-beam approximation, where θ_B is the operating Bragg angle, $\mathbf{k}^{(i)}$ (i =1, 2) is the wave number vector of i-th branch, **g** is the diffraction vector, s is the excitation error, ξ_g is the extinction distance and $\gamma^{(i)}$ (i =1, 2) is the eigenvector of the Bloch states. $D^{(i)}$ is the Bloch state excited on the dispersion surface determined by the incident electron direction and the boundary condition.

Figure 3 Excitation parameters of the two types of Bloch waves as functions of the excitation error.

Figure 4 Unit cell structure of GaAs, projected in the direction inclined by 12° from the [011] direction, and compatible with the experimental conditions of the plot in Figure 5.

Figure 5 Experimental (open symbols) and simulated (solid line) characteristic X-ray intensity variations as functions of incident electron-tilt-angle in the [100] direction for GaAs. The theoretical simulations were performed at 200 kV by incorporating the Bloch waves for $|\mathbf{g}| < 50$ nm^{-1} and $s_g < 0.3$ nm^{-1} (the number of Bloch waves incorporated was ~160) with a sample thickness of 90 nm and a convergence semiangle of 1 mrad.

Figure 6 Experimental geometry of diffraction pattern for site-selective EELS. The EELS detector is placed off-axis from the transmitted beam **O,** parallel to the Kikuchi line to enhance the localization of the energy loss event with the electron channelling boundary condition maintained.

Figure 7 Schematic of two STEM beam control modes: (a) scanning the focused beam parallel to the sample surface, and (b) parallel beam rocking about a pivot point on the sample surface.

Figure 8 Electron channelling patterns (ECPs) and ionized channelling pattern (ICPs) of Ba-L, T-K_α, and O-K_α emissions from $BaTiO_3$, obtained by beam-rocking around [100] (a) and [110]

zone axes (b). The projected atomic structures along the corresponding zone axis directions are attached.

Figure 9 (a) Atomic structure of GaAs projected along [310]. (b) Calculated X-ray ICPs around [310] of Ga-K, As-K, and Si-K and 1:1 linear combination of Ga-K and As-K ICPs for sample thicknesses of 25, 50, 100, and 150 nm of GaAs containing 1 at.% Si equally occupying Ga and As sites.

Figure 10 Deduced c_{Si} (a) and $f_{i,Si}$ (i = Ga or As) (b) found by applying St-ALCHEMI to the ICP dataset of Figure 9. Cliff-Lorimer k-factors, k_{Ga}/k_{Si} and k_{As}/k_{Si} are adjusted to yield the correct values for c_{Si} (=1) and $f_{i,Si}$ (= 0.5) at 25 nm thickness.

Figure 11 Change in c_{Si} (a) and $f_{i,Si}$ with variation of k_{Ga}/k_{Si}, estimated using Eq. (36) and (37).

Figure 12 Unit cell structure of Ca_2SnO_4 (a) and cation-oxygen polyhedra around Ca (7-coordinated) and Sn (6-coordinated) (b).

Figure13 ECPs and corresponding X-ray ICPs of Ca-K_α, Sn-L, O-K_α, O-K_α, Eu-L, and Y-L emissions obtained from $Ca_{1.8}Eu_{0.2}Y_{0.2}Sn_{0.8}O_4$ by beam-rocking about [100] zone axis.

Figure 14 Unit cell structure of Sr-M-type ferrite, $SrFe_{12}O_{19}$ projected along the $[1\bar{1}0]$ zone axis. Different Fe-sites are indicated.

Figure 15 (a) Bright-field transmission electron microscopy (TEM) image of a crystal grain in which ECP/ICPs were acquired. (b) Corresponding transmission electron diffraction pattern.

Figure 16 ECP and corresponding X-ray ICPs for Fe-K, Sr-L, O-K, Co-K, and La-L lines of $Sr_{0.8}La_{0.2}Fe_{11.4}Co_{0.2}O_{19}$, respectively.

Figure 17 Comparison between the experimental Fe-K ICP (a) and the calculated Fe-K ICP (b). (c) Comparison between experimental and calculated intensity profiles along the $[00\bar{1}]$ direction, projected to the [110] direction.

Figure 18 Comparison between the theoretical site-specific X-ray ICPs (upper row) and extracted experimental X-ray ICPs of Fe-K_α emission for the seven different Fe sites.

Figure 19 (a) Experimental Co-K incoherent ionization channelling pattern (ICP) and (b) the corresponding fitted Co-K ICP. (c) The residual image of the multivariate linear regression. (d) Comparison between the intensity histograms of the residual image and the noise image. The residual image and the noise image (high-frequency components) in (a) are indicated by the fitting error (open circles) and the experimental noise (open boxes), respectively.

Figure 20 (a) A set of Mn-L_3 HARECES data with the incident beam tilted in the range $0 \leq k_x/g_{400} \leq 3$. Thick grey lines are the expected primary peak positions from Mn^{2+} and Mn^{4+}, as a visual guide. (b) HARECXS data of Mn-K_α taken concurrently with the HARECES data in (a). (c) Corresponding diffraction pattern at $k_x/g_{400} = 0$.

Figure 21 Site-specific spectra (solid lines) of Mn-L_3 for the resolved octahedral (top: Mn_{oct}-L_3) and tetrahedral sites (bottom: Mn_{tet}-L_3). The Mn-L_3 ELNES of MnO_2 (Mn^{4+}: broken lines on top) is overlaid over each Mn_{oct}-L_3, and the reference spectra of Mn^{2+} and Mn^{3+} (broken lines) are also overlaid over Mn_{tet}-L_3 for comparison. Each spectrum was normalized by its integrated intensity. The orange solid lines at the bottom are the best-fit curves to Mn_{tet}-L_3 by the two spectra (broken lines), with weighting as described in the text.

Table 1. Derived parameters (defined in text) of the samples of $Ca_{2-x}Eu_xSn_{1-y}Y_yO_4$ where (x, y) = (0.2, 0.0) and (0.2, 0.2), respectively, refer to Eu20 and Eu20Y20

Sample	Dopant	α_{Ca}	α_{Sn}	f_{Ca}	f_{Sn}	c_x (x = Eu or Y)
Eu20	Eu	1.71±0.001	0.083±0.001	0.57±0.001	0.43±0.002	0.061±0.001
Eu20Y20	Eu	0.162±0.001	0.077±0.001	0.78±0.003	0.22±0.008	0.088±0.006
	Y	0.040±0.002	0.265±0.009	0.28±0.002	0.72±0.001	0.118±0.004

Table 2. Seven candidate models derived from the neutron diffraction and Rietveld analysis, showing the fraction of the occupation site of Co. The symbols 2a, 2b, $4f_1$, $4f_2$, and 12k indicate Wyckoff notation for the Fe sites.

Model #	2a	2b	$4f_1$	$4f_2$	12k
1	-	-	1.00	-	-
2	-	-	-	-	1.00
3	0.35	-	0.65	-	-
4	0.31	-	-	-	0.69
5	-	-	0.88	0.12	-
6	-	-	0.47	-	0.53
7	0.22	-	0.38	-	0.40

Table 3. Derived parameters of the statistical atom location for $Sr_{0.8}La_{0.2}Fe_{11.4}Co_{0.2}O_{19}$.

		f_{Co}^j	
	α_j	k-factor of NSS software	Theoretical k-factor
2a	0.0630(35)	0.23(1)	0.22(1)
2b	0.0079(34)	0.03(1)	0.03(1)
$4f_1$	0.0808(22)	0.57(2)	0.56(1)
$4f_2$	0.0083(15)	0.06(1)	0.06(1)
12k	0.0050(7)	0.11(2)	0.11(2)
c_{Co} [atom%]		0.83(4)	0.82(4)

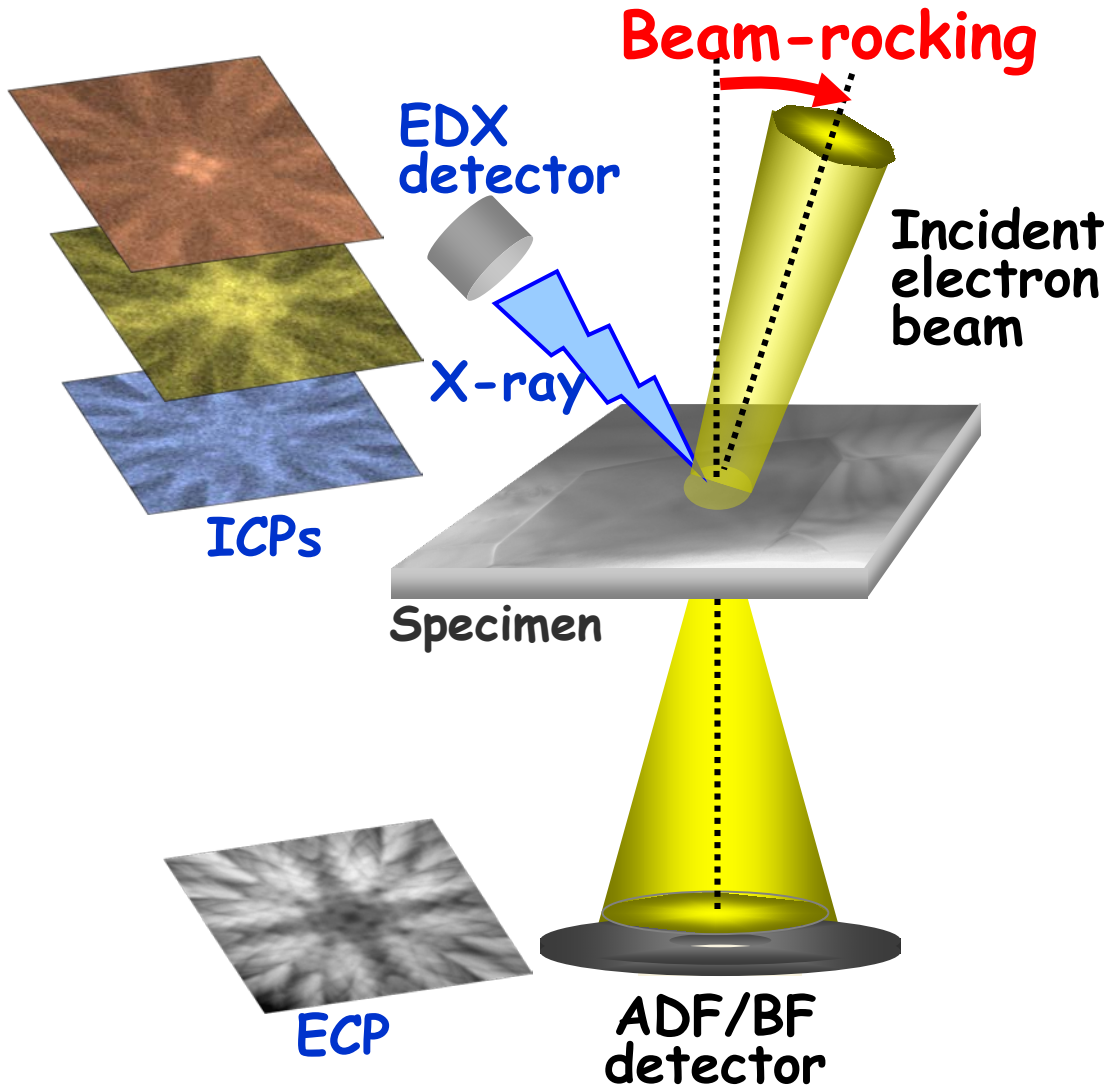

Graphic abstract

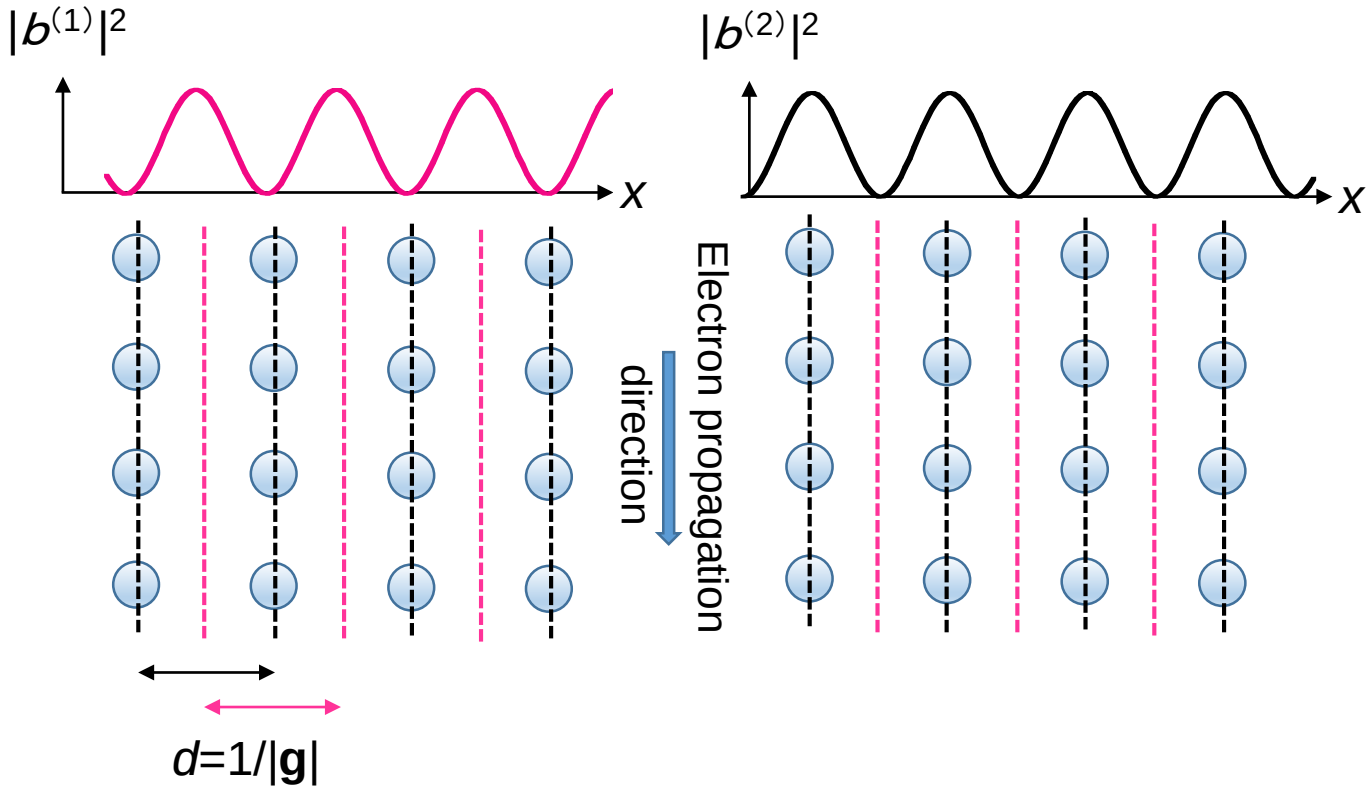

Figure 1 Schematic diagrams of the two types of Bloch wave intensity distributions at the reflecting position in a simple cubic lattice in the direction normal to the reflecting planes. The electron current flow is parallel to the reflecting planes.

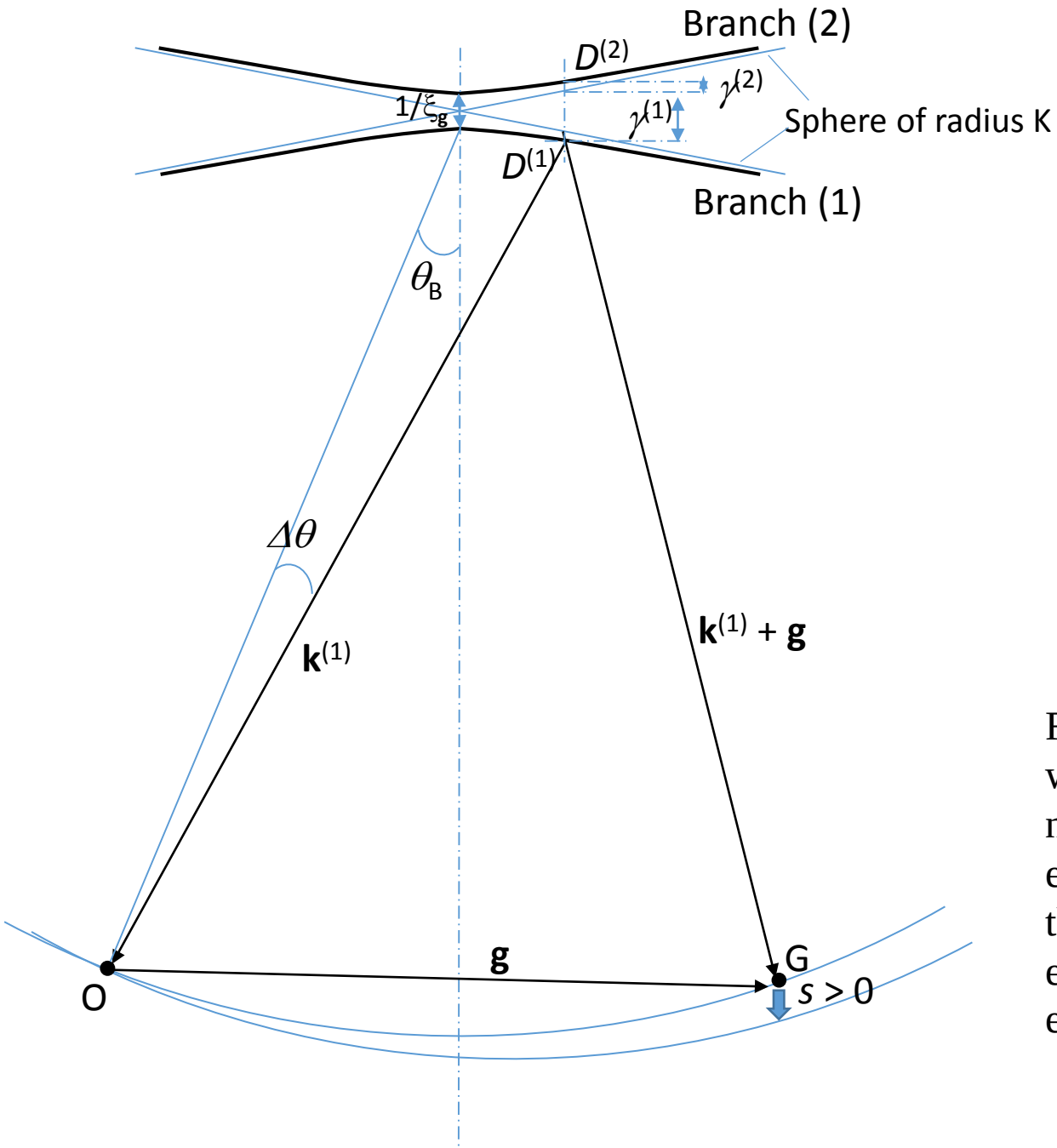

Figure 2 Dispersion surface in the two-beam approximation, where θ_B is the operating Bragg angle, $\mathbf{k}^{(i)}$ (i =1, 2) is the wave number vector of i-th branch, $\mathbf{g}$ is the diffraction vector, s is the excitation error, ξ_g is the extinction distance and $\gamma^{(i)}$ (i =1, 2) is the eigenvector of the Bloch states. $D^{(i)}$ is the Bloch state excited on the dispersion surface determined by the incident electron direction and the boundary condition.

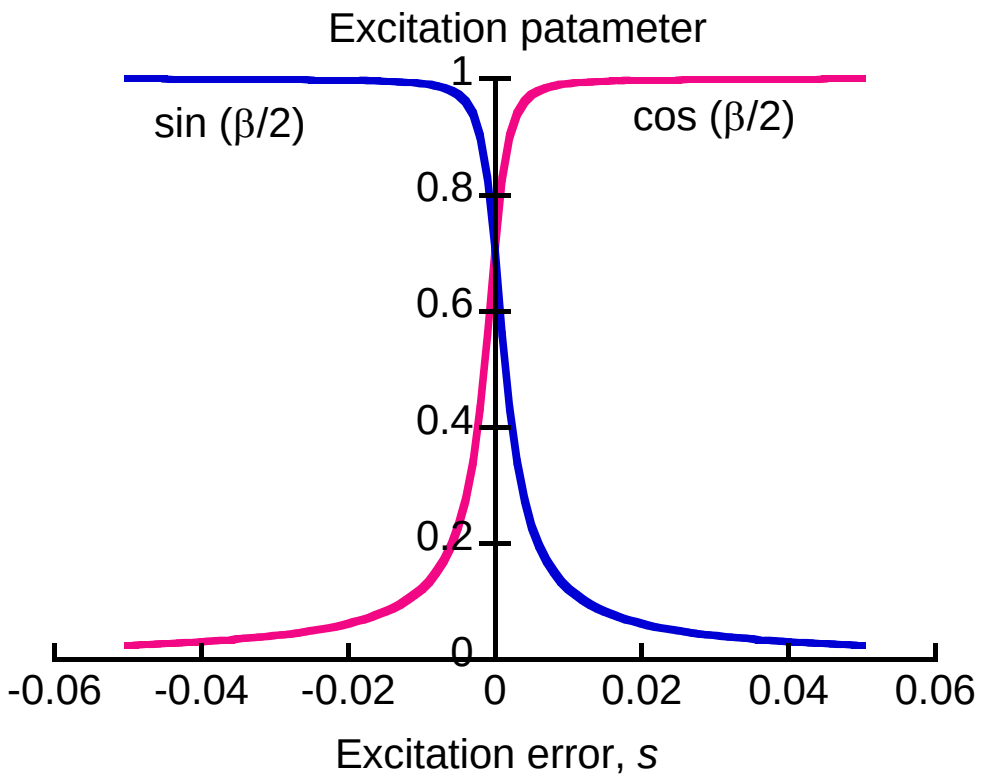

Figure 3 Excitation parameters of the two types of Bloch waves as functions of the excitation error.

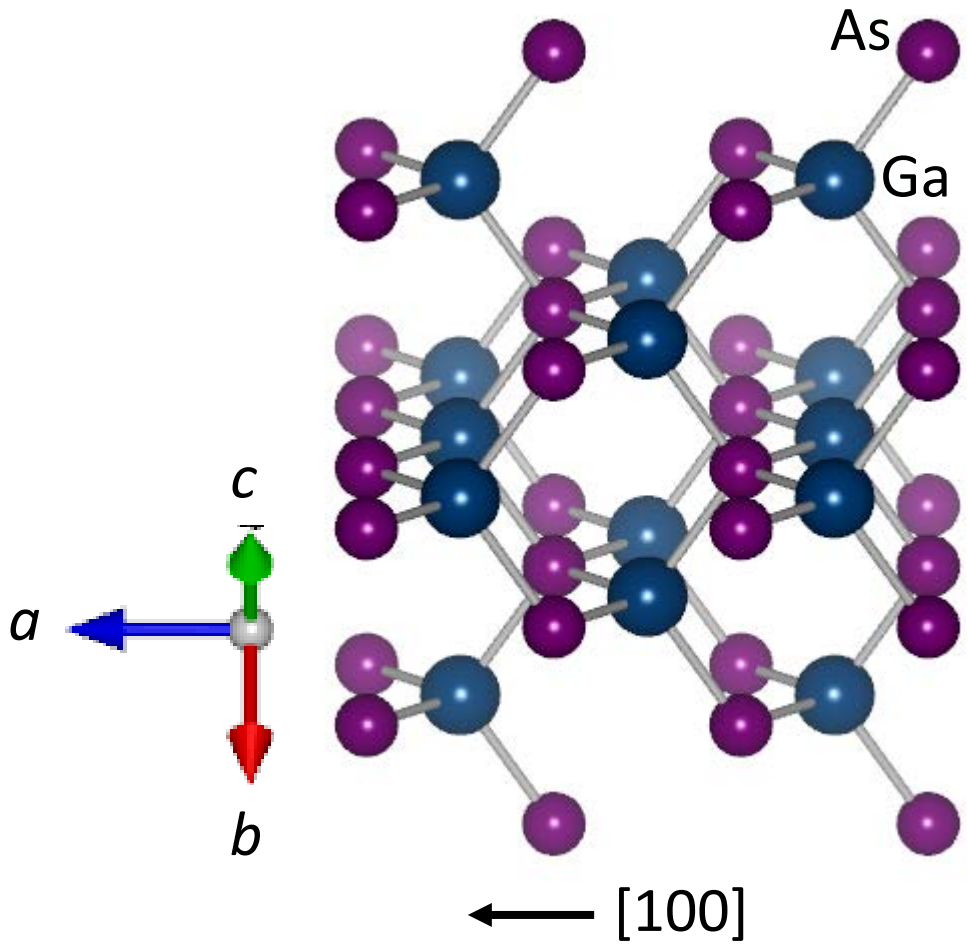

Figure 4 Unit cell structure of GaAs, projected in the direction inclined by 12° from the [011] direction, and compatible with the experimental conditions of the plot in Figure 5.

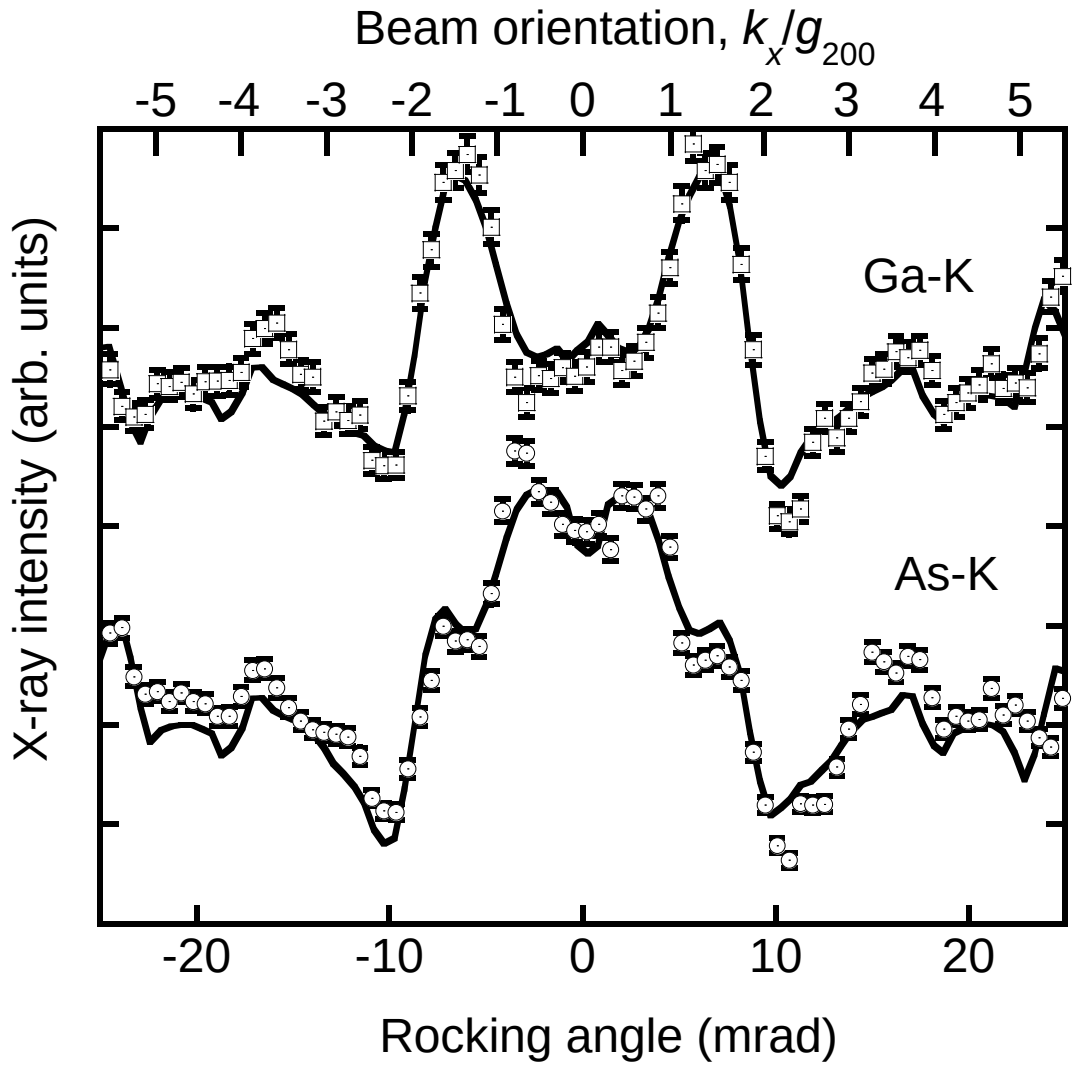

Figure 5 Experimental (open symbols) and simulated (solid line) characteristic X-ray intensity variations as functions of incident electron-tilt-angle in the [100] direction for GaAs. The theoretical simulations were performed at 200 kV by incorporating the Bloch waves for $|\mathbf{g}| < 50$ nm^{-1} and $s_g < 0.3$ nm^{-1} (the number of Bloch waves incorporated was ~160) with a sample thickness of 90 nm and a convergence semiangle of 1 mrad.

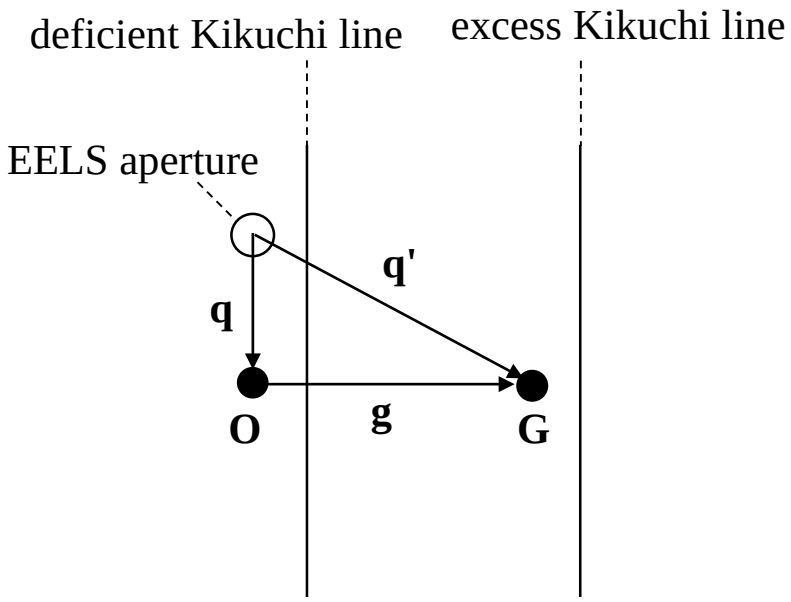

Figure 6 Experimental geometry of diffraction pattern for site-selective EELS. The EELS detector is placed off-axis from the transmitted beam **O,** parallel to the Kikuchi line to enhance the localization of the energy loss event with the electron channelling boundary condition maintained.

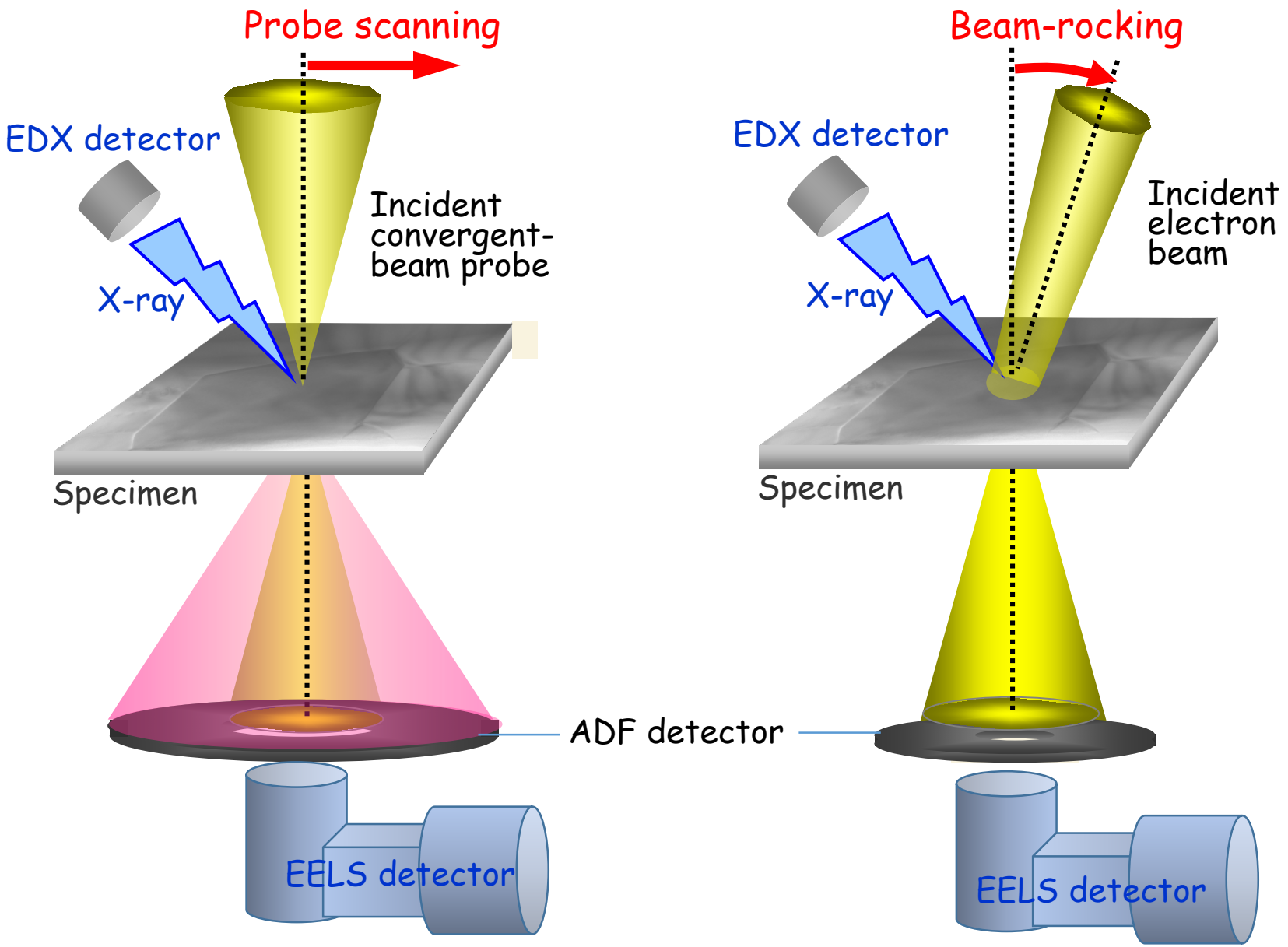

Figure 7 Schematic of two STEM beam control modes: (a) scanning the focused beam parallel to the sample surface, and (b) parallel beam rocking about a pivot point on the sample surface.

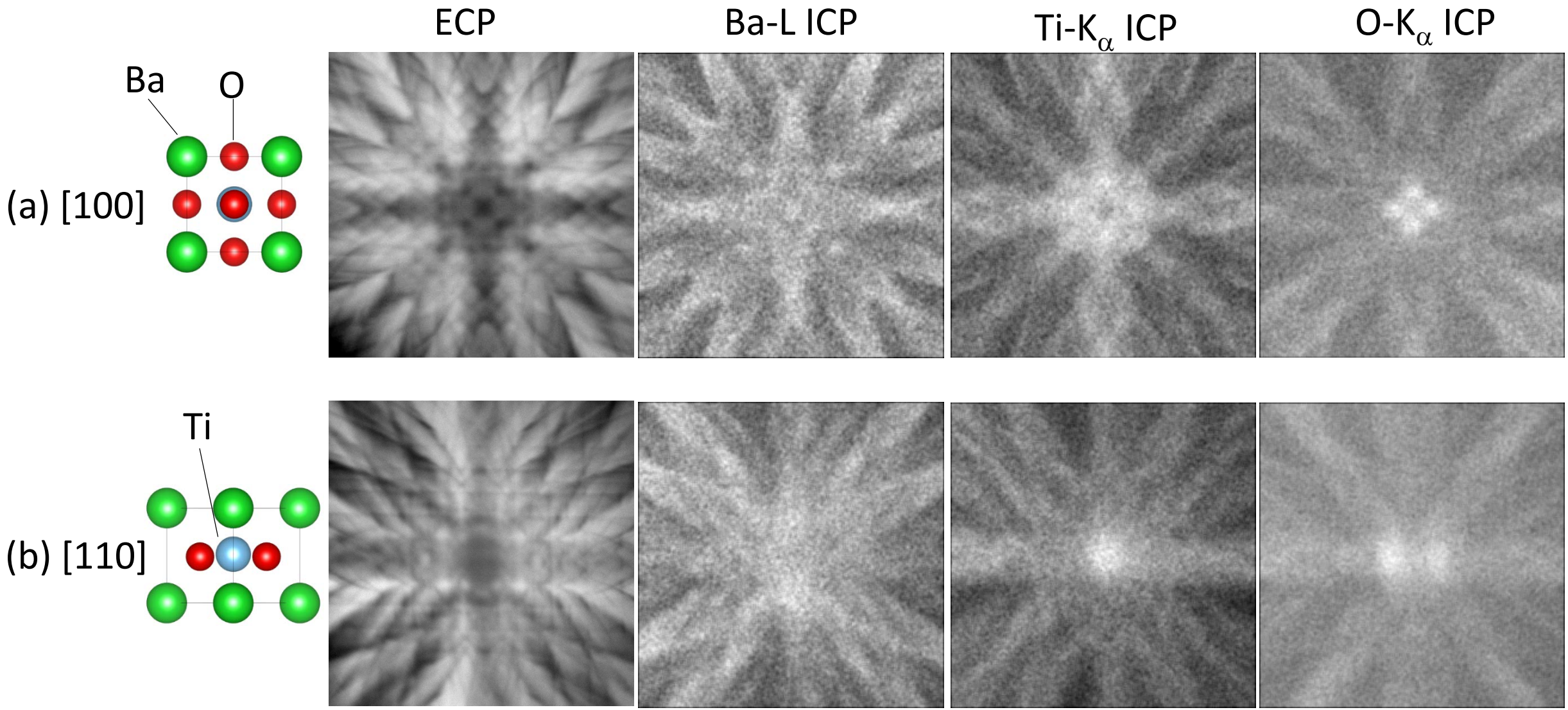

Figure 8 Electron channelling patterns (ECPs) and ionized channelling pattern (ICPs) of Ba-L, T-K_α, and O-K_α emissions from $BaTiO_3$, obtained by beam-rocking around [100] (a) and [110] zone axes (b). The projected atomic structures along the corresponding zone axis directions are attached.

(a)

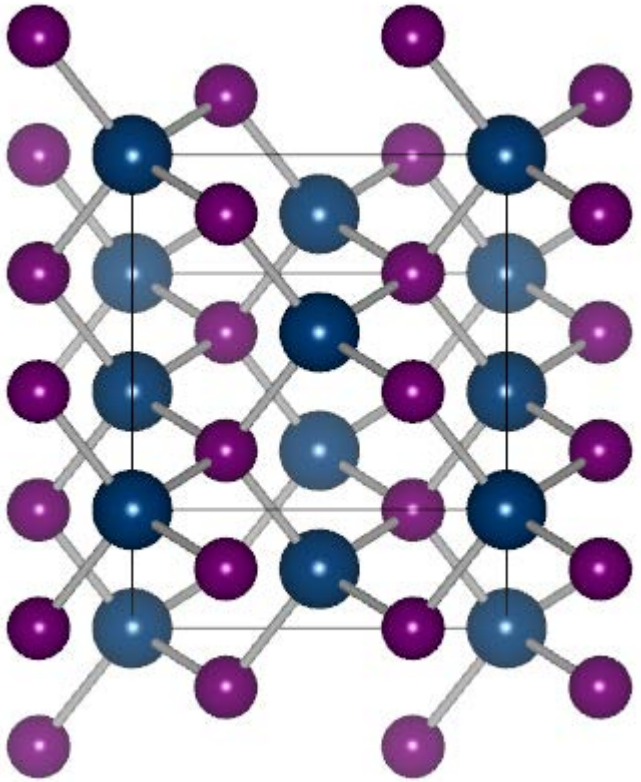

(b)

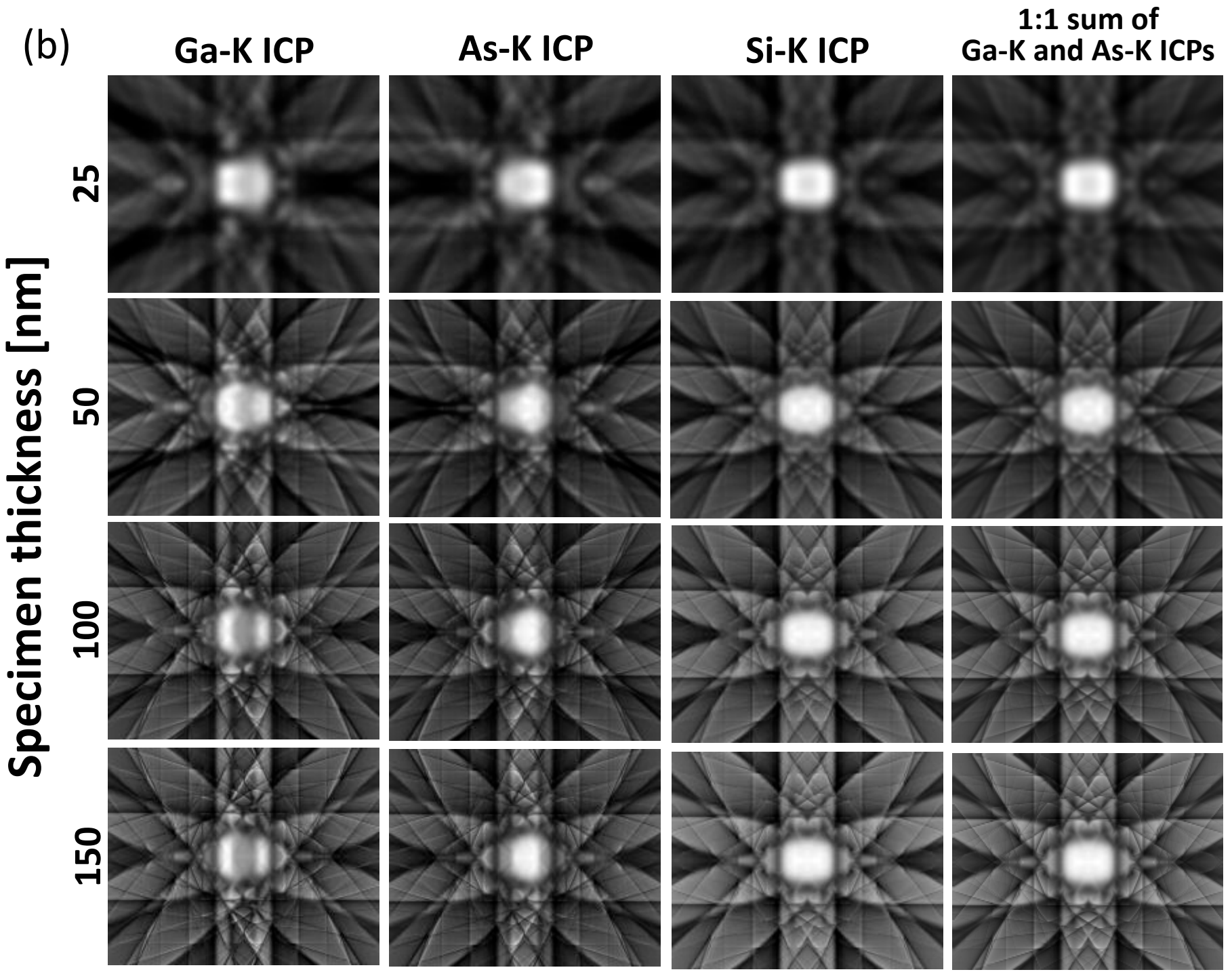
Ga-K ICP
As-K ICP
Si-K ICP
1:1 sum of Ga-K and As-K ICPs
Specimen thickness [nm]
25
50
100
150

Figure 9

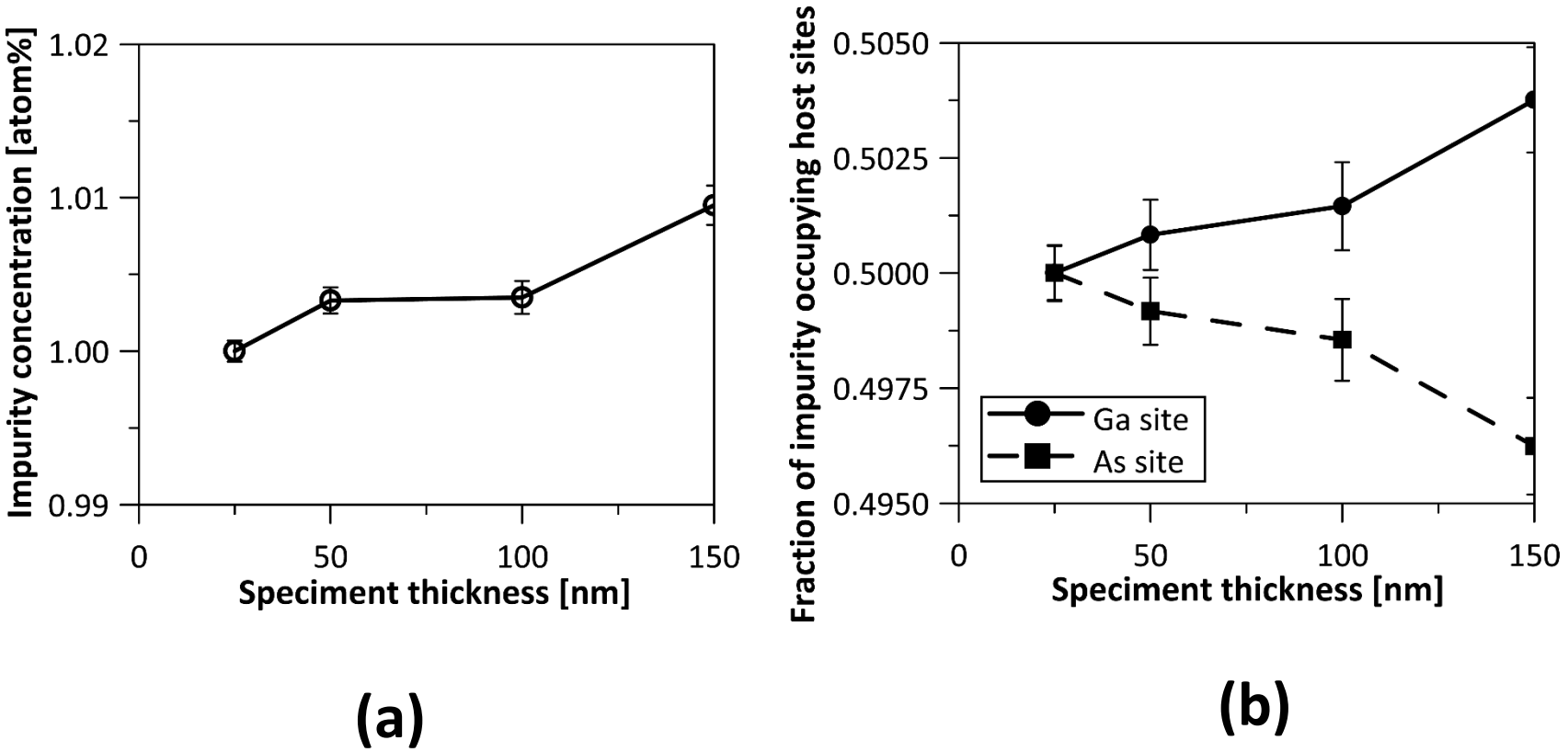

Figure 10 Deduced c_{Si} (a) and $f_{i,Si}$ (i = Ga or As) (b) found by applying St-ALCHEMI to the ICP dataset of Figure 9. Cliff-Lorimer k-factors, k_{Ga}/k_{Si} and k_{As}/k_{Si} are adjusted to yield the correct values for c_{Si} (=1) and $f_{i,Si}$ (= 0.5) at 25 nm thickness.

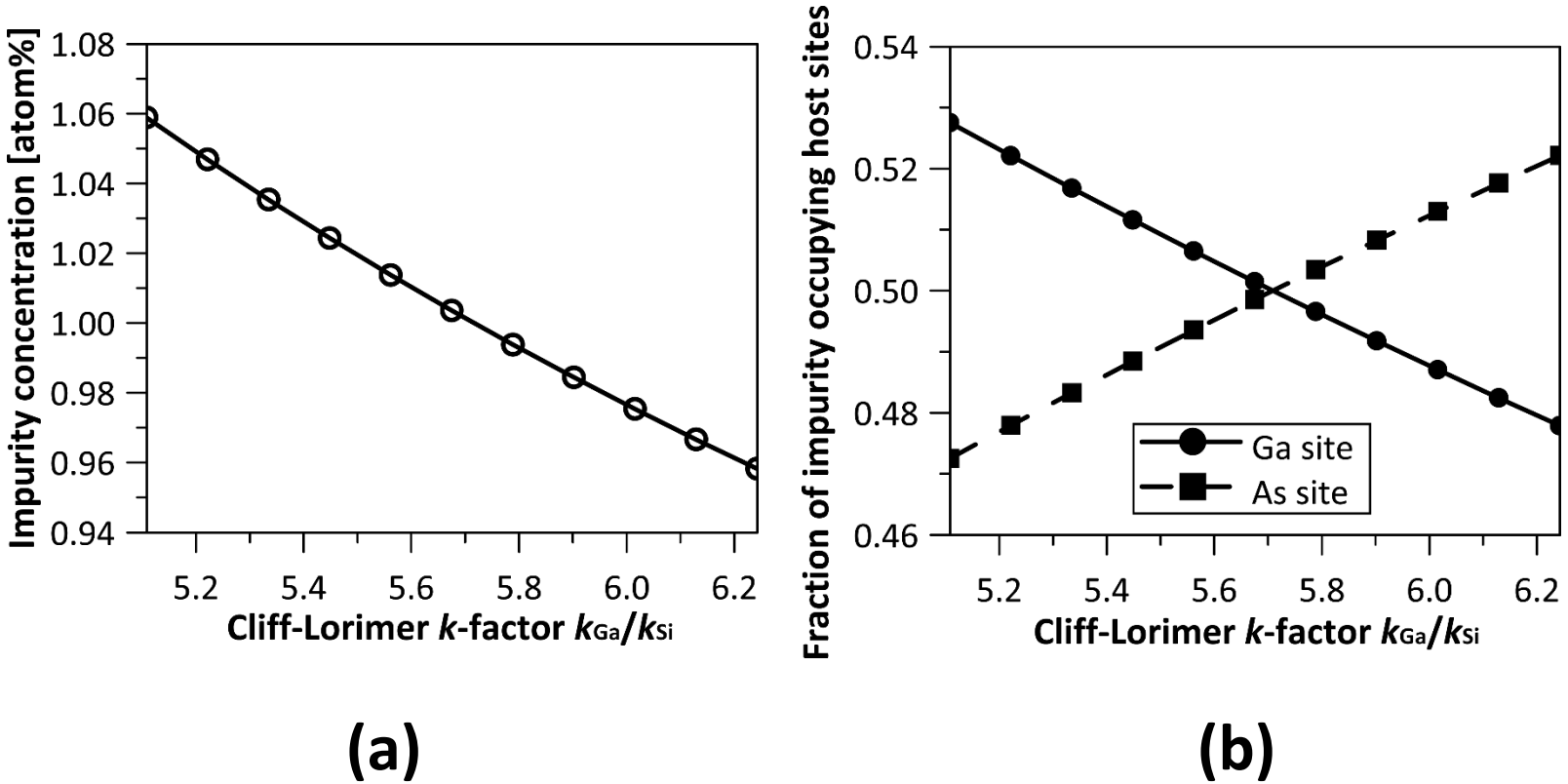

Figure 11 Change in c_{Si} (a) and $f_{i,Si}$ with variation of k_{Ga}/k_{Si}, estimated using Eq. (36) and (37).

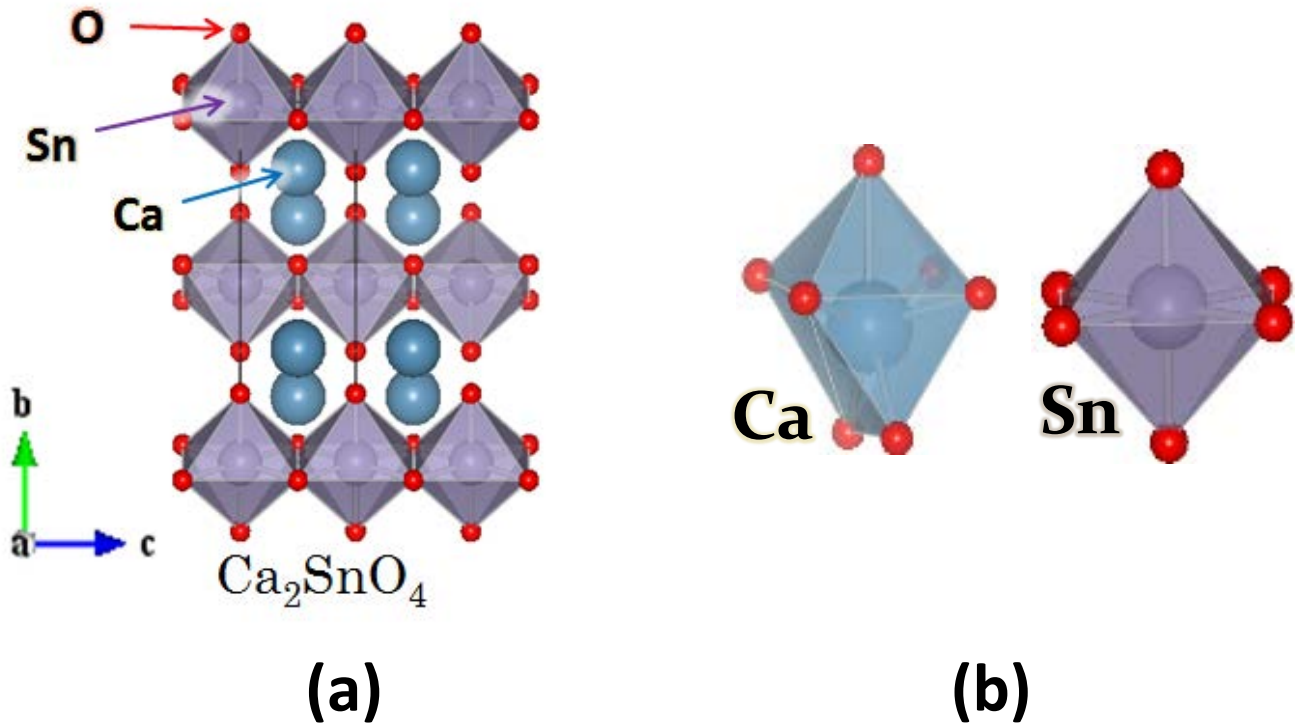

Figure 12 Unit cell structure of Ca_2SnO_4 (a) and cation-oxygen polyhedra around Ca (7-coordinated) and Sn (6-coordinated) (b).

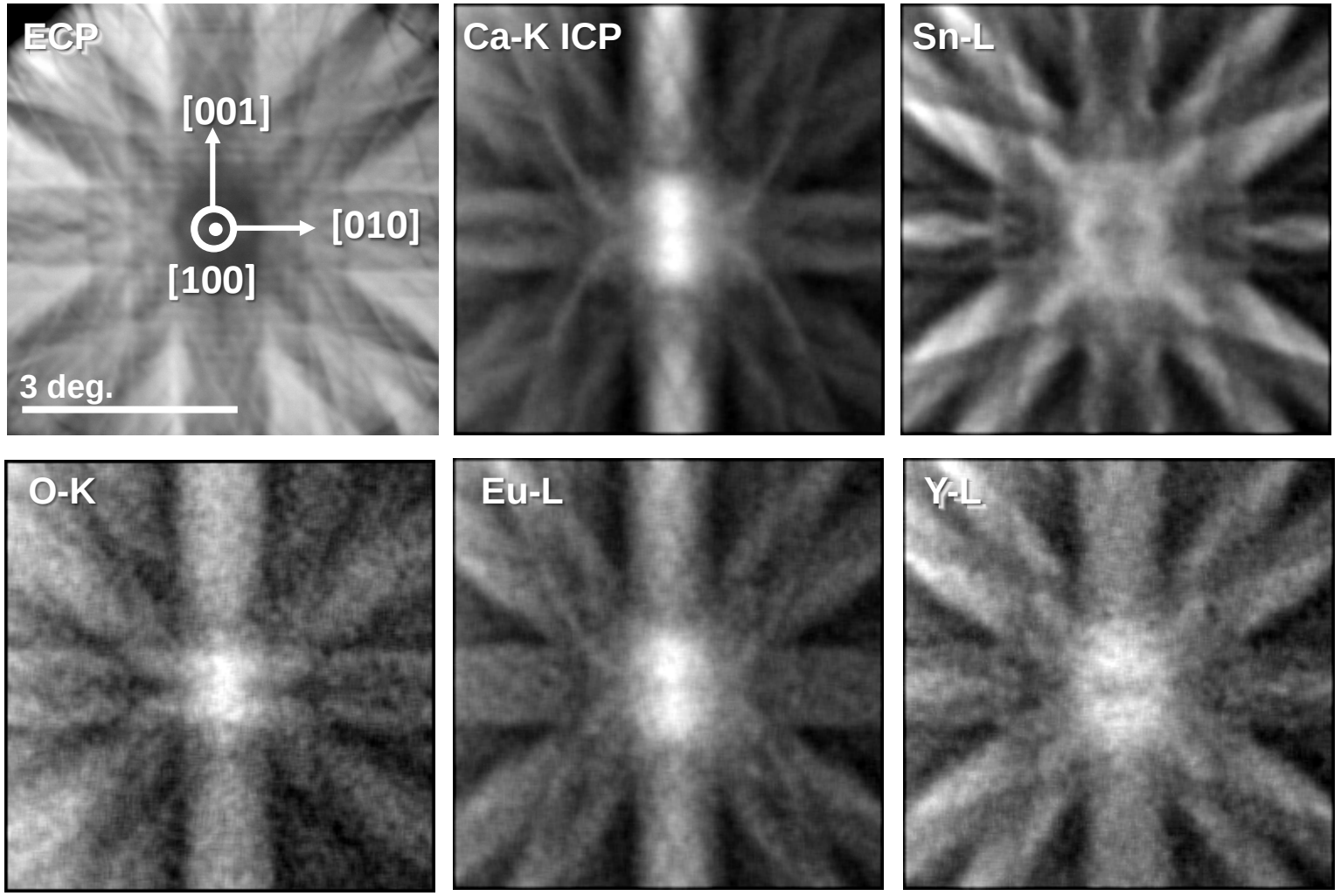

Figure13 ECPs and corresponding X-ray ICPs of Ca-K_α, Sn-L, O-K_α, O-K_α, Eu-L, and Y-L emissions obtained from $Ca_{1.8}Eu_{0.2}Y_{0.2}Sn_{0.8}O_4$ by beam-rocking about [100] zone axis.

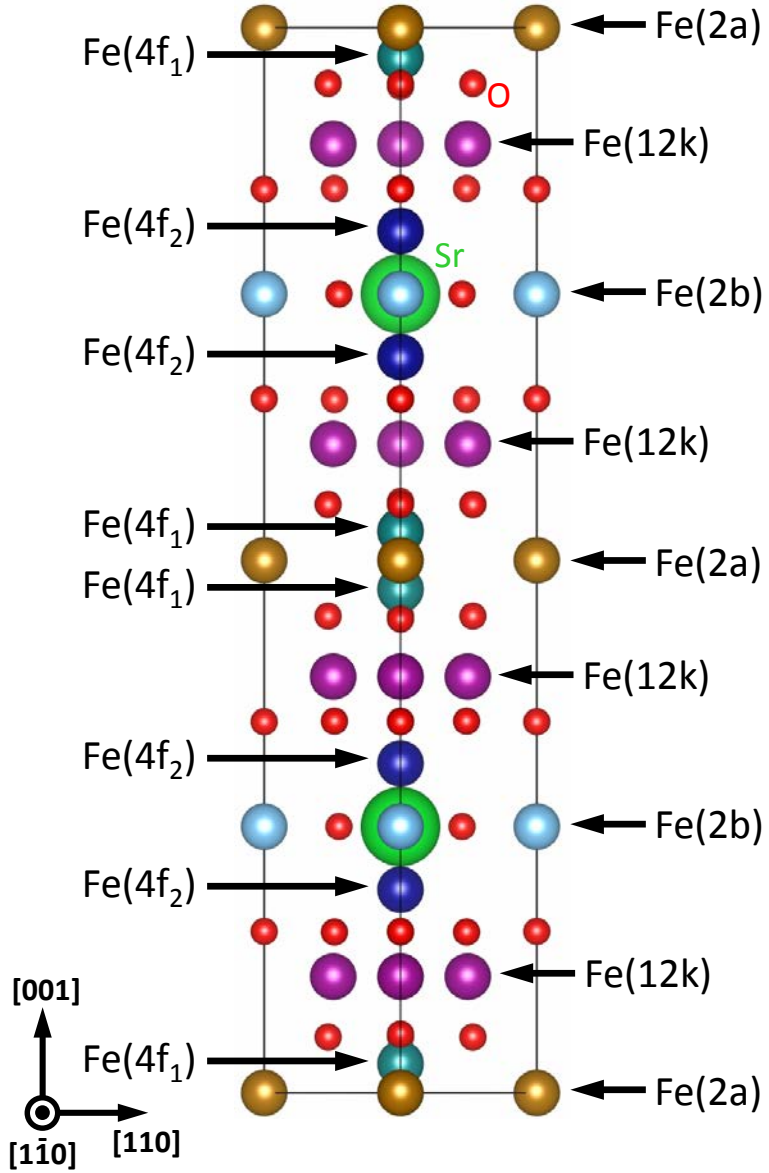

Figure 14 Unit cell structure of Sr-M-type ferrite, $SrFe_{12}O_{19}$ projected along the [1$\bar{1}$0] zone axis. Different Fe-sites are indicated.

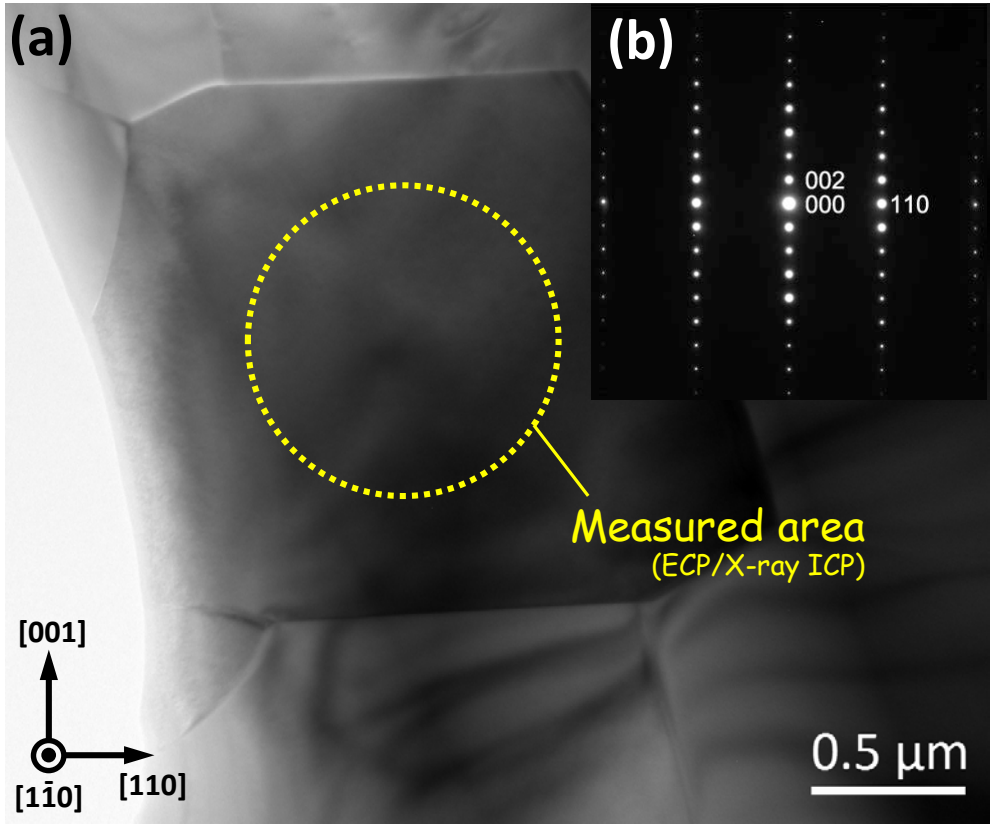

Figure 15 (a) Bright-field transmission electron microscopy (TEM) image of a crystal grain in which ECP/ICPs were acquired. (b) Corresponding transmission electron diffraction pattern.

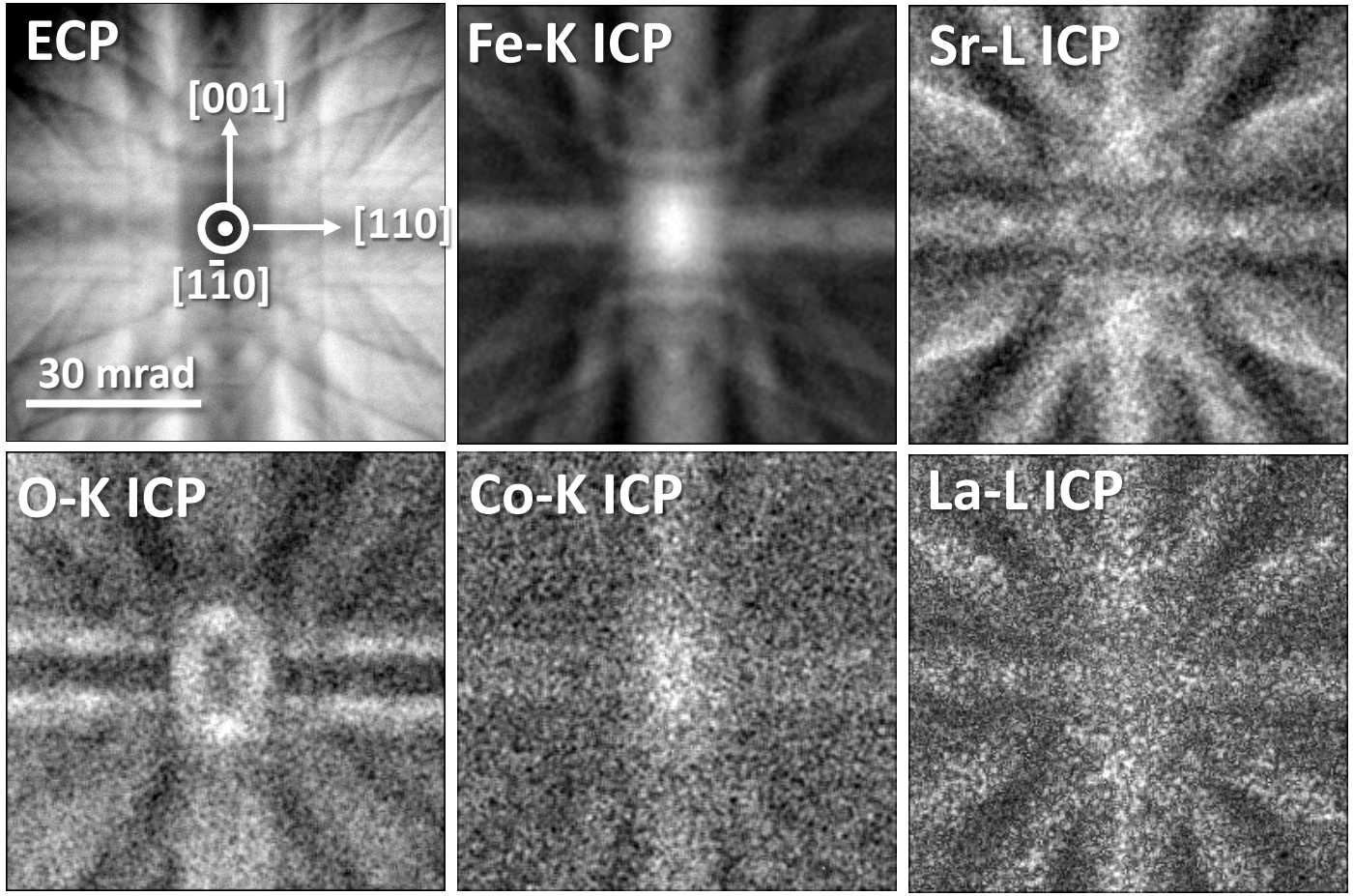

Figure 16 ECP and corresponding X-ray ICPs for Fe-K, Sr-L, O-K, Co-K, and La-L lines of $Sr_{0.8}La_{0.2}Fe_{11.4}Co_{0.2}O_{19}$, respectively.

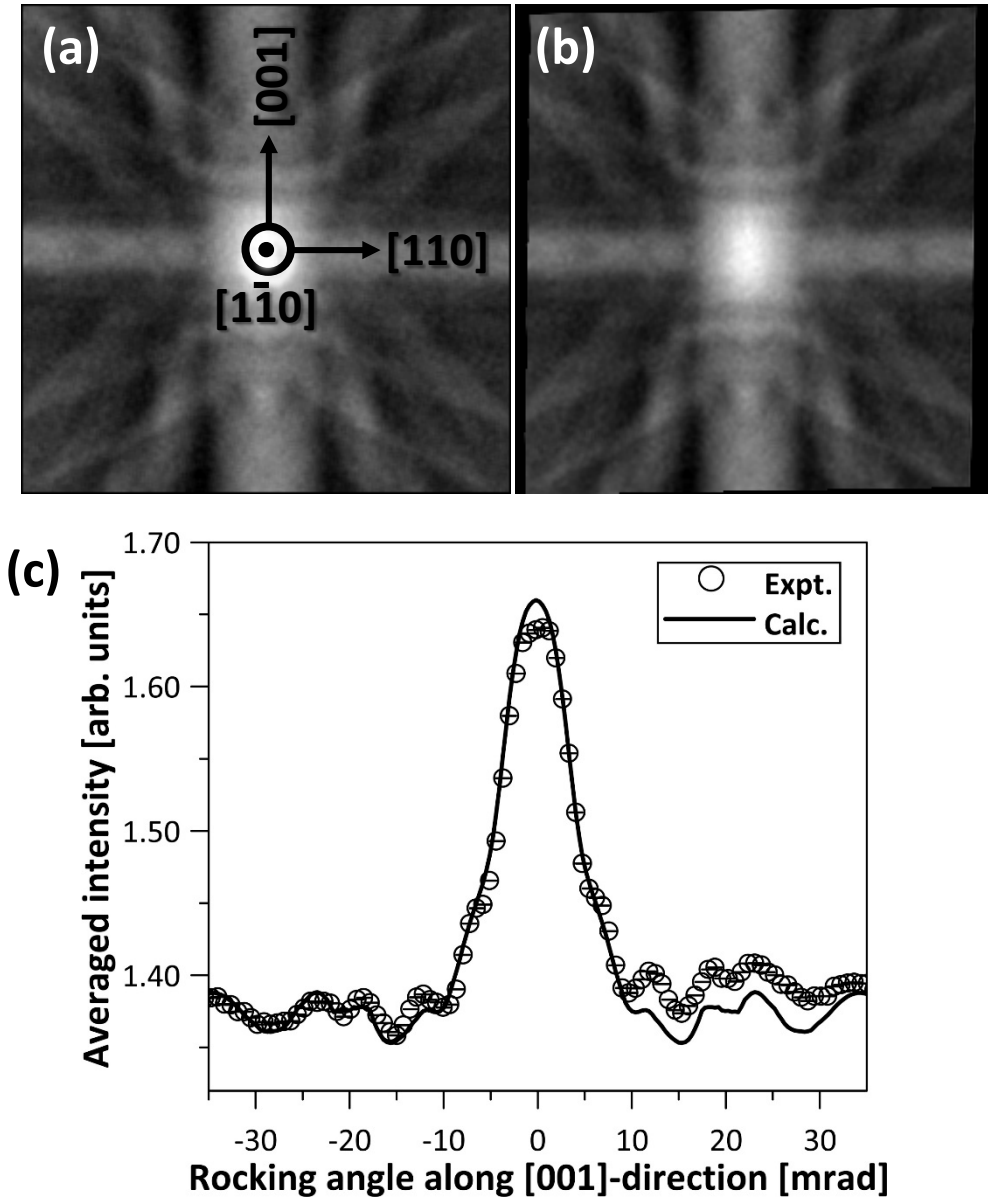

Figure 17 Comparison between the experimental Fe-K ICP (a) and the calculated Fe-K ICP (b). (c) Comparison between experimental and calculated intensity profiles along the [00$\bar{1}$] direction, projected to the [110] direction.

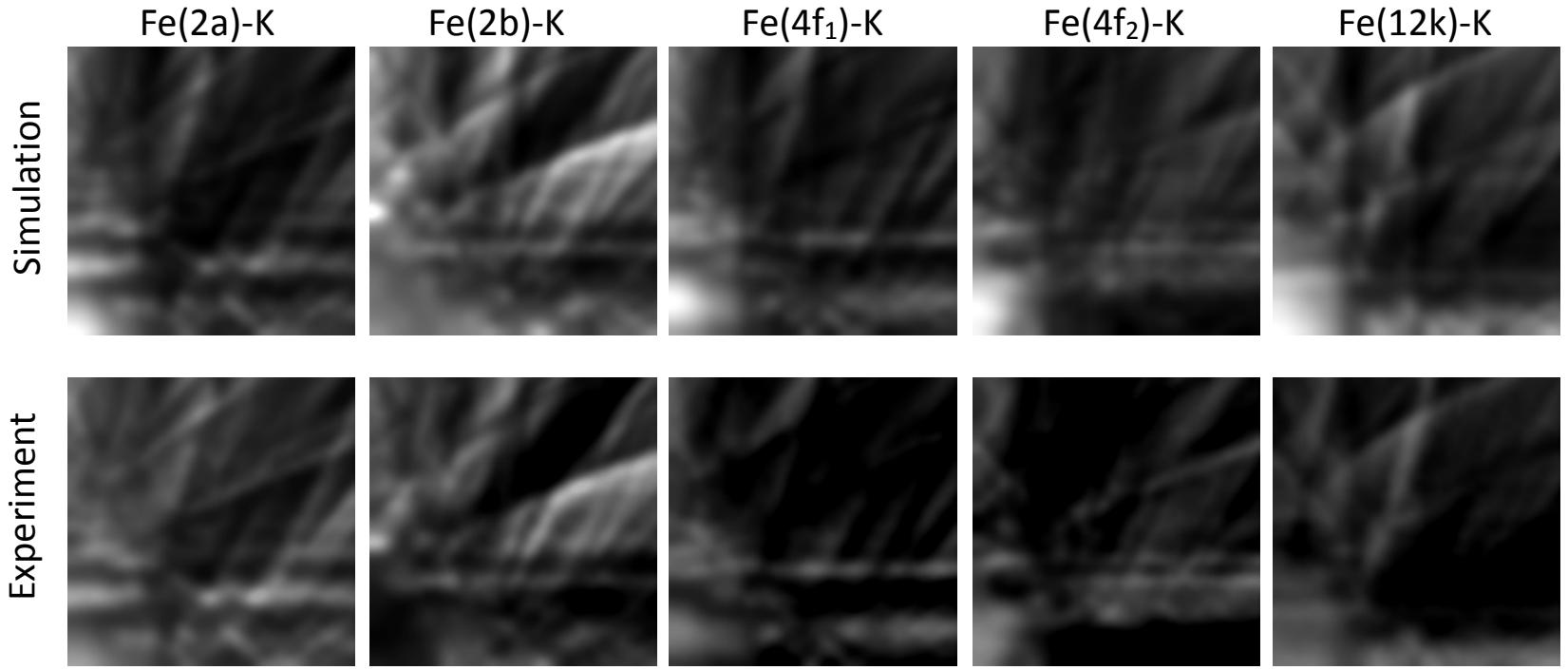

Figure 18 Comparison between the theoretical site-specific X-ray ICPs (upper row) and extracted experimental X-ray ICPs of Fe-K_α emission for the seven different Fe sites.

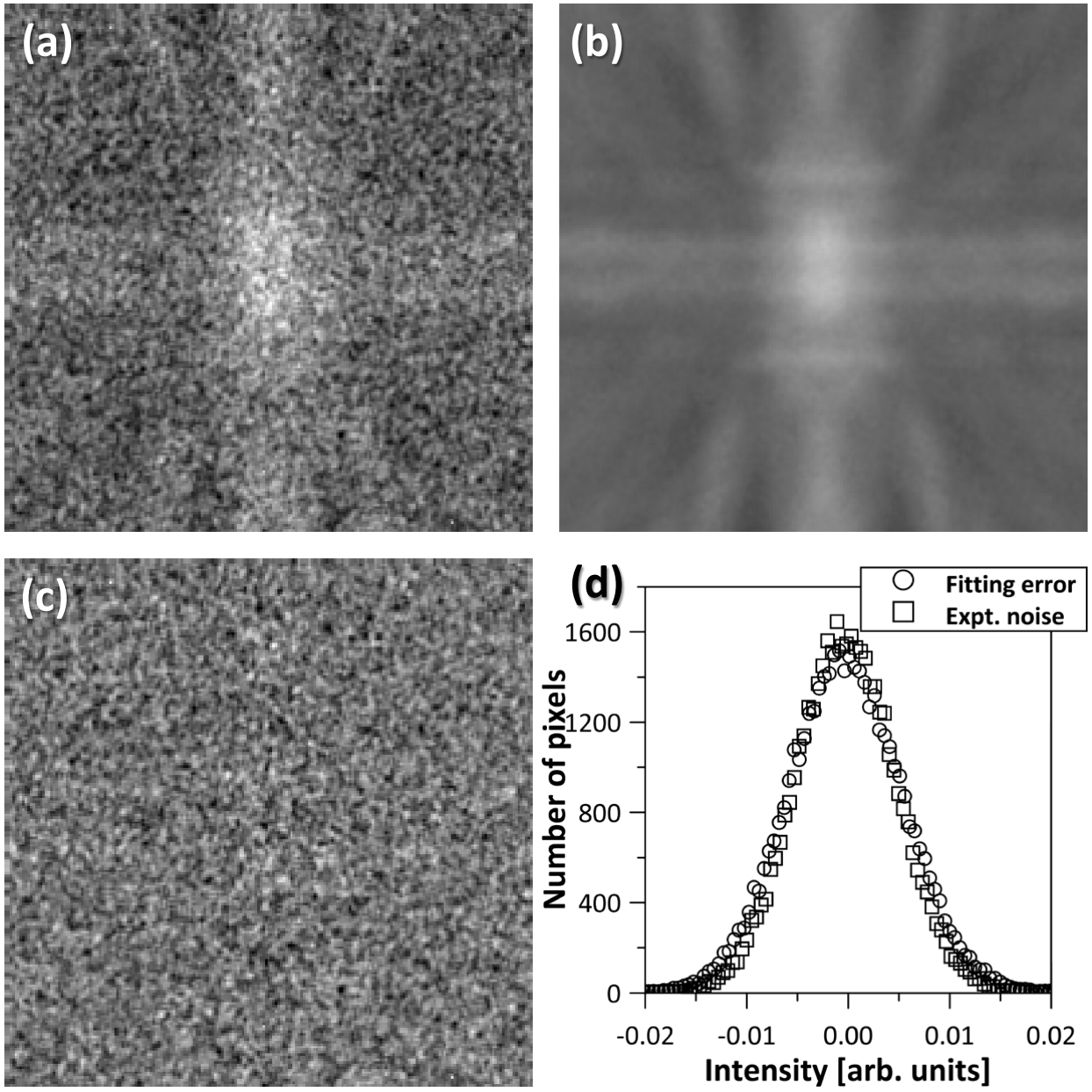

Figure 19 (a) Experimental Co-K incoherent ionization channelling pattern (ICP) and (b) the corresponding fitted Co-K ICP. (c) The residual image of the multivariate linear regression. (d) Comparison between the intensity histograms of the residual image and the noise image. The residual image and the noise image (high-frequency components) in (a) are indicated by the fitting error (open circles) and the experimental noise (open boxes), respectively.

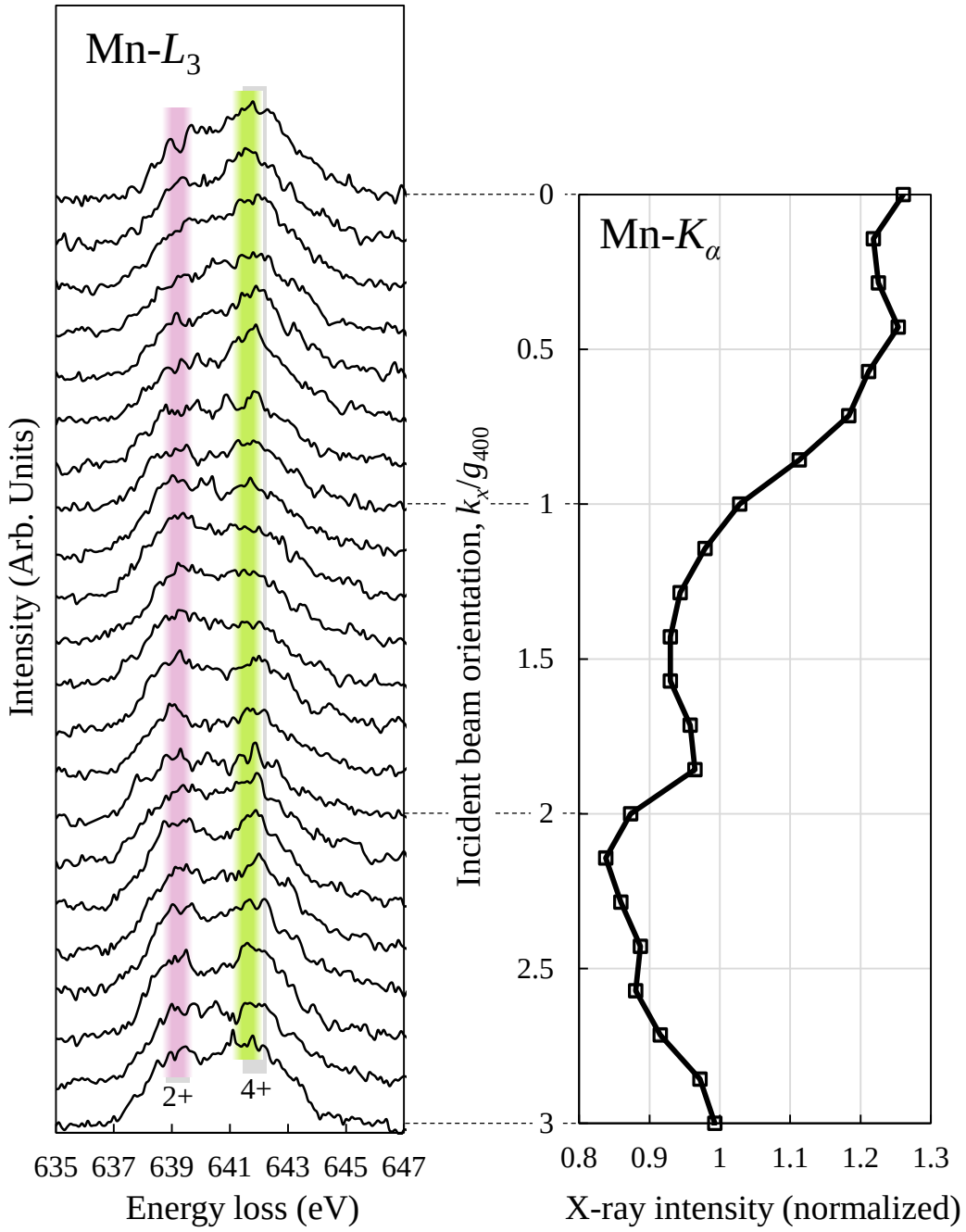

(a) (b)

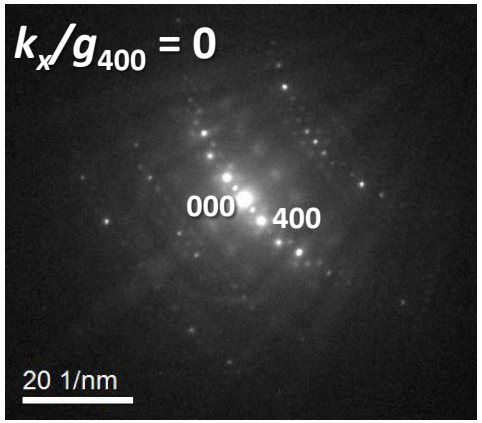

(c)

Figure 20 (a) A set of Mn-L_3 HARECES data with the incident beam tilted in the range $0 \leq k_x/g_{400} \leq 3$. Thick grey lines are the expected primary peak positions from Mn^{2+} and Mn^{4+}, as a visual guide. (b) HARECXS data of Mn-K_α taken concurrently with the HARECES data in (a). (c) Corresponding diffraction pattern at $k_x/g_{400} = 0$.

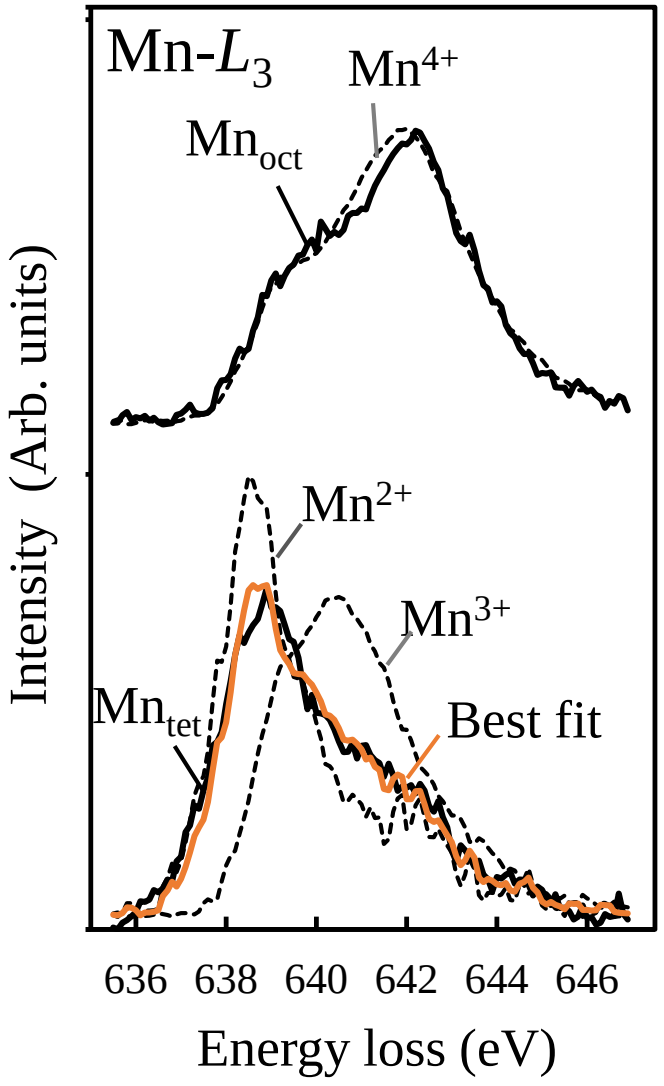

Figure 21 Site-specific spectra (solid lines) of Mn-L_3 for the resolved octahedral (top: Mn_{oct}-L_3) and tetrahedral sites (bottom: Mn_{tet}-L_3). The Mn-L_3 ELNES of MnO_2 (Mn^{4+}: broken lines on top) is overlaid over each Mn_{oct}-L_3, and the reference spectra of Mn^{2+} and Mn^{3+} (broken lines) are also overlaid over Mn_{tet}-L_3 for comparison. Each spectrum was normalized by its integrated intensity. The orange solid lines at the bottom are the best-fit curves to Mn_{tet}-L_3 by the two spectra (broken lines), with weighting as described in the text.